

AD\_\_\_\_\_

Award Number: DAMD17-00-1-0455

TITLE: Scanning Microwave Induced Acoustic Tomography

PRINCIPAL INVESTIGATOR: Lihong Wang, Ph.D.

CONTRACTING ORGANIZATION: Texas Engineering Experiment Station/The  
Texas A&M University System  
College Station, Texas 77843-3000

REPORT DATE: October 2002

TYPE OF REPORT: Annual

PREPARED FOR: U.S. Army Medical Research and Materiel Command  
Fort Detrick, Maryland 21702-5012

DISTRIBUTION STATEMENT: Approved for Public Release;  
Distribution Unlimited

The views, opinions and/or findings contained in this report are those of the author(s) and should not be construed as an official Department of the Army position, policy or decision unless so designated by other documentation.

20030319 039

**REPORT DOCUMENTATION PAGE**Form Approved  
OMB No. 074-0188

Public reporting burden for this collection of information is estimated to average 1 hour per response, including the time for reviewing instructions, searching existing data sources, gathering and maintaining the data needed, and completing and reviewing this collection of information. Send comments regarding this burden estimate or any other aspect of this collection of information, including suggestions for reducing this burden to Washington Headquarters Services, Directorate for Information Operations and Reports, 1215 Jefferson Davis Highway, Suite 1204, Arlington, VA 22202-4302, and to the Office of Management and Budget, Paperwork Reduction Project (0704-0188), Washington, DC 20503

<b>1. AGENCY USE ONLY (Leave blank)</b>		<b>2. REPORT DATE</b> October 2002	<b>3. REPORT TYPE AND DATES COVERED</b> Annual (1 Oct 01 - 30 Sep 02)	
<b>4. TITLE AND SUBTITLE</b> Scanning Microwave Induced Acoustic Tomography			<b>5. FUNDING NUMBERS</b> DAMD17-00-1-0455	
<b>6. AUTHOR(S)</b> Lihong Wang, Ph.D.				
<b>7. PERFORMING ORGANIZATION NAME(S) AND ADDRESS(ES)</b> Texas Engineering Experiment Station/The Texas A&M University System College Station, Texas 77843-3000  <b>E-Mail:</b> lwang@tamu.edu			<b>8. PERFORMING ORGANIZATION REPORT NUMBER</b>	
<b>9. SPONSORING / MONITORING AGENCY NAME(S) AND ADDRESS(ES)</b> U.S. Army Medical Research and Materiel Command Fort Detrick, Maryland 21702-5012			<b>10. SPONSORING / MONITORING AGENCY REPORT NUMBER</b>	
<b>11. SUPPLEMENTARY NOTES</b>				
<b>12a. DISTRIBUTION / AVAILABILITY STATEMENT</b>  Approved for Public Release; Distribution Unlimited			<b>12b. DISTRIBUTION CODE</b>	
<b>13. ABSTRACT (Maximum 200 Words)</b> Since October 2001, we have published three peer-reviewed journal articles in <u>IEEE Transactions on Medical Imaging</u> —a top imaging journal, published one conference proceedings article, and delivered 9 invited talks. The combination of ultrasound and microwave has provided us a unique opportunity for early-cancer imaging with high resolution and high contrast. We have made significant technical progress in thermoacoustic imaging including data acquisition and imaging reconstruction. Specifically, our accomplishments include (1) an exact and an approximate time-domain reconstruction algorithm for thermoacoustic tomography in a spherical geometry was derived and published, (2) an exact frequency-domain reconstruction algorithm for thermoacoustic tomography in a planar geometry was derived and published, (3) an exact frequency-domain reconstruction algorithm for thermoacoustic tomography in a cylindrical geometry was derived and published, and (4) high-resolution and high-contrast images were obtained and published. The reconstruction is an inverse source problem similar to that in PET (positron emission tomography); however, the reconstruction in PET is based on geometric optics whereas the reconstruction in thermoacoustic imaging is based on diffractive/wave optics. We have successfully imaged biological tissue with high resolution and high contrast. We will advance this				
<b>14. SUBJECT TERMS</b> breast cancer, detection, photoacoustic effect, microwave, ultrasonography			<b>15. NUMBER OF PAGES</b> 39	
			<b>16. PRICE CODE</b>	
<b>17. SECURITY CLASSIFICATION OF REPORT</b> Unclassified	<b>18. SECURITY CLASSIFICATION OF THIS PAGE</b> Unclassified	<b>19. SECURITY CLASSIFICATION OF ABSTRACT</b> Unclassified	<b>20. LIMITATION OF ABSTRACT</b> Unlimited	

## Table of Contents

Cover.....	1
SF 298.....	2
Table of Contents.....	3
Introduction.....	4
Body.....	4
Key Research Accomplishments.....	13
Reportable Outcomes.....	13
Conclusions.....	15
References.....	15
Appendices (23 pages).....	16

## Introduction

A novel imaging technology, scanning microwave-induced-acoustic tomography, will be developed for breast imaging. X-ray mammography and ultrasonography are the current clinical tools for breast-cancer screening and detection. Mammography is the “gold standard”, however, uses ionizing radiation and has difficulties imaging pre-menopausal breasts, which are radiographically dense. Ultrasonography is an adjunct tool to x-ray mammography and cannot detect many of the nonpalpable tumors. The cure rate of breast cancers is improved if they are detected early. To provide a new non-invasive, non-ionizing diagnostic tool for detection of early breast cancers, we will develop real-time microwave-induced-acoustic tomography for breast imaging. Microwave-induced-acoustic tomography is based on the photoacoustic effect, generation of acoustic wave by deposition of short-pulse electromagnetic energy safely into biological tissues. The microwave for this technology is short-pulsed, and its power is within the IEEE safety limits. The microwave-induced acoustic wave is then detected with an ultrasonic detector for imaging. The contrast between tumors and normal tissues in the microwave regime is significantly better than other imaging modalities. Cancerous breast tissues are found to be 2-5 times more strongly absorbing than surrounding normal breast tissues in the microwave, which has been attributed to an increase in bound water and sodium within malignant cells. However, pure-microwave imaging is fundamentally limited to poor resolution (on the order of 10 mm) because of the large wavelength of microwave. Ultrasonic imaging has good resolution (on the order of 1 mm) but has a poor contrast between tumors and normal tissues. Microwave-induced-acoustic tomography combines the contrast advantage of pure-microwave imaging and the resolution advantage of pure-ultrasonic imaging, therefore, has the potential for detection of early breast cancers and for assessing and monitoring treatments as well.

## Body

In this section, we present our study of pulsed-microwave-induced thermoacoustic tomography in biological tissues. A short-pulsed microwave source was used to irradiate the tissue samples, and the thermoacoustic waves excited by thermoelastic expansion were then measured by a wide-band ultrasonic transducer along a circular path that encloses the sample under study. The acquired data were then used to reconstruct the microwave absorption distribution. Both an exact reconstruction solution and an approximate modified backprojection algorithm were derived. Experiments demonstrated that the images calculated by the backprojection method agreed with the original samples very well, and the spatial resolution in reconstruction was as good as 0.5 millimeter (500 micrometers).

### Introduction to thermoacoustic tomography

In thermoacoustic tomography, a short-pulsed microwave source is used to irradiate the tissue. Absorbed microwave energy causes thermoelastic expansion and radiates thermoacoustic waves from within the irradiate tissue. The relatively long wavelength of the microwave, e.g., ~3 cm at 3 GHz in tissues, serves to illuminate the tissue homogeneously. The microwave heating must be rapid to produce thermoacoustics waves; in other words, static temperature distribution or

slow heating cannot produce thermoacoustic waves. A wide-band ultrasonic transducer can then be employed to acquire the thermoacoustic signals excited by thermoelastic expansion, which carries the microwave absorption property of the tissue. The ultrasonic transducer is very sensitive in detecting small vibrations from an object that are caused by weak energy absorption.

The key problem with this technique is how to determine the microwave absorption distribution from the measured data, i.e., how to map the inhomogeneity of the tissue. One approach is to use focused ultrasonic transducers to localize the thermoacoustic sources in linear or sector scans and then construct the images directly from the data as is often done in pulse-echo ultrasonography. An alternative method is to use wide-band unidirectional point detectors to acquire thermoacoustic data and then reconstruct the microwave absorption distribution. To date, we have not seen an exact inverse solution for this specific problem, although some researchers have arrived at approximate reconstruction algorithms, such as the weighted delay-and-sum method, the optimal statistical approach, and the Radon transform in far field approximation.

Based on spherical harmonic functions, we first deduced an exact solution of the problem in the three-dimensional case, which can be carried out in the frequency domain. We assume that the wide-band unidirectional ultrasonic transducer is set on a spherical surface, which encloses the sample under investigation. The data acquired from different directions are sufficient to allow us to reconstruct the microwave absorption distribution. In our case, the diameter of the sphere of detection is much larger than the ultrasonic wavelength. Next, an approximate algorithm is deduced, which is a modified backprojection of a quantity related with the thermoacoustic pressure. This approximate algorithm can be carried out in the time domain and is much faster than the exact solution. We have also tested a set of tissue samples. These experiments demonstrate that the images calculated by the modified backprojection method agree with the original samples very well. Moreover, the images have both the high contrast associated with pure-microwave imaging and the 0.5-millimeter spatial resolution associated with pure-ultrasound imaging.

## Theory of thermoacoustic tomography

### *Fundamentals of thermoacoustics*

Thermoacoustic theory has been discussed in many literature reviews such as. Here, we briefly review only the fundamental equations. If the microwave pumping pulse duration is much shorter than the thermal diffusion time, thermal diffusion can be neglected; consequently, the thermal equation becomes

$$\rho C_p \frac{\partial}{\partial t} T(\mathbf{r}, t) = H(\mathbf{r}, t), \quad (1)$$

where  $\rho$  is the density,  $C_p$  is the specific heat,  $T(\mathbf{r}, t)$  is the temperature rise due to the energy pumping pulse, and  $H(\mathbf{r}, t)$  is the heating function defined as the thermal energy per time and volume deposited by the energy source. We are interested in tissue with inhomogeneous microwave absorption but a homogeneous acoustic property. The two basic acoustic generation equations in a homogeneous medium are the linear inviscid force equation

$$\rho \frac{\partial^2}{\partial t^2} \mathbf{u}(\mathbf{r}, t) = -\nabla p(\mathbf{r}, t) \quad (2)$$

and the expansion equation

$$\nabla \cdot \mathbf{u}(\mathbf{r}, t) = -\frac{p(\mathbf{r}, t)}{\rho c^2} + \beta T(\mathbf{r}, t) \quad (3)$$

where  $\beta$  is the isobaric volume expansion coefficient,  $c$  is the sound speed,  $\mathbf{u}(\mathbf{r}, t)$  is the acoustic displacement and  $p(\mathbf{r}, t)$  is the acoustic pressure.

Combining the above three equations, the pressure  $p(\mathbf{r}, t)$  produced by the heat source  $H(\mathbf{r}, t)$  obeys the following equation

$$\nabla^2 p(\mathbf{r}, t) - \frac{1}{c^2} \frac{\partial^2}{\partial t^2} p(\mathbf{r}, t) = -\frac{\beta}{C_p} \frac{\partial}{\partial t} H(\mathbf{r}, t). \quad (4)$$

The above equation is a typical scalar Helmholtz equation. The solutions based on Green's function can be found in the literature of physics or mathematics. A general form can be expressed as

$$p(\mathbf{r}, t) = \frac{\beta}{4\pi C_p} \iiint \frac{d^3 r'}{|\mathbf{r} - \mathbf{r}'|} \left. \frac{\partial H(\mathbf{r}', t')}{\partial t'} \right|_{t' = t - \frac{|\mathbf{r} - \mathbf{r}'|}{c}}. \quad (5)$$

The heating function can be written as the product of a spatial absorption function and a temporal illumination function:

$$H(\mathbf{r}, t) = A(\mathbf{r})I(t). \quad (6)$$

Thus,  $p(\mathbf{r}, t)$  can be expressed as

$$p(\mathbf{r}, t) = \frac{\beta}{4\pi C_p} \iiint \frac{d^3 r'}{|\mathbf{r} - \mathbf{r}'|} A(\mathbf{r}')I'(t'). \quad (7)$$

### Exact reconstruction theory

We first solve the problem where the pulse pumping is a Dirac delta function as

$$I(t) = I_0 \delta(t). \quad (8)$$

Suppose the detection point on the spherical surface  $\mathbf{r} = \mathbf{r}_0$ , which encloses the sample (Fig. 1). By dropping the primes, the pressure equation may be written as

$$p(\mathbf{r}_0, t) = \eta \iiint d^3 r A(\mathbf{r}) \frac{\delta'(t - \frac{|\mathbf{r}_0 - \mathbf{r}|}{c})}{4\pi |\mathbf{r}_0 - \mathbf{r}|}, \quad (9)$$

where  $\eta = \frac{\beta I_0}{C_p}$ . The inverse problem is to reconstruct the absorption distribution  $A(\mathbf{r})$  from a set of data  $p(\mathbf{r}_0, t)$  measured at position  $\mathbf{r}_0$ . Taking the Fourier transform on variable  $t$  of the above equation and denoting  $k = \frac{\omega}{c}$ , we get

$$\tilde{p}(\mathbf{r}_0, \omega) = -i\omega\eta \iiint d^3 r A(\mathbf{r}) \frac{\exp(ik|\mathbf{r}_0 - \mathbf{r}|)}{4\pi |\mathbf{r}_0 - \mathbf{r}|}, \quad (10)$$

where following Fourier transform pair exists:

$$\tilde{p}(\mathbf{r}_0, \omega) = \int_{-\infty}^{+\infty} p(\mathbf{r}_0, t) \exp(i\omega t) dt, \quad (11)$$

$$p(\mathbf{r}_0, t) = \frac{1}{2\pi} \int_{-\infty}^{+\infty} \tilde{p}(\mathbf{r}_0, \omega) \exp(-i\omega t) d\omega. \quad (12)$$

The exact inverse solution to the pressure equation (Eq. 9) can be derived on the basis of the spherical harmonic function:

$$A(\mathbf{r}) = \frac{1}{4\pi^2 \eta c} \iint_{\Omega_0} d\Omega_0 \int_{-\infty}^{+\infty} dk \tilde{p}(\mathbf{r}_0, \omega) \sum_{m=0}^{\infty} \frac{(2m+1) j_m(kr)}{h_m^{(1)}(kr_0)} P_m(\mathbf{n} \cdot \mathbf{n}_0), \quad (13)$$

where  $\mathbf{n} = \mathbf{r}/r$ ,  $\mathbf{n}_0 = \mathbf{r}_0/r_0$ ,  $j_l(\cdot)$  and  $h_l^{(1)}(\cdot)$  are the spherical Bessel and Hankel functions, respectively;  $P_l(\cdot)$  represents Legendre polynomial. This inverse solution involves summation of a series and may take much time to compute. Therefore, it is desirable to further simplify the solution.

#### Modified backprojection

In the experiments, the detection radius  $r_0$  is much larger than the wavelengths of the thermoacoustic waves that are useful for imaging. Because the low-frequency components of the thermoacoustic signal do not significantly contribute to the spatial resolution, they can be removed by a filter. Therefore, we can assume  $|k|r_0 \gg 1$  and use the asymptotic form of the Hankel function to simplify the above exact inverse solution. The following two identities are involved:

$$\frac{\exp(-ik|\mathbf{r}_0 - \mathbf{r}|)}{4\pi|\mathbf{r}_0 - \mathbf{r}|} = \frac{-ik}{4\pi} \sum_{m=0}^{\infty} (2m+1) j_m(kr) h_m^{(2)}(kr_0) P_m(\mathbf{n} \cdot \mathbf{n}_0); \quad (14)$$

$$\text{When } |k|r_0 \gg 1, \quad h_m^{(1)}(kr_0) \approx \frac{1}{h_m^{(2)}(kr_0)} \left( \frac{1}{(kr_0)^2} + O\left(\frac{1}{(kr_0)^4}\right) \right), \quad (15)$$

where  $h_l^{(2)}(\cdot)$  is the spherical Hankel function of the second kind. After some mathematical operations, the approximate inverse solution becomes

$$A(\mathbf{r}) = -\frac{r_0^2}{2\pi\eta c^3} \iint_{\Omega_0} d\Omega_0 \frac{1}{|\mathbf{r}_0 - \mathbf{r}|} \left. \frac{\partial p(\mathbf{r}_0, t)}{\partial t} \right|_{t=\frac{|\mathbf{r}_0 - \mathbf{r}|}{c}} \quad (16)$$

i.e.,

$$A(\mathbf{r}) = -\frac{r_0^2}{2\pi\eta c^4} \iint_{\Omega_0} d\Omega_0 \frac{1}{t} \left. \frac{\partial p(\mathbf{r}_0, t)}{\partial t} \right|_{t=\frac{|\mathbf{r}_0 - \mathbf{r}|}{c}}. \quad (17)$$

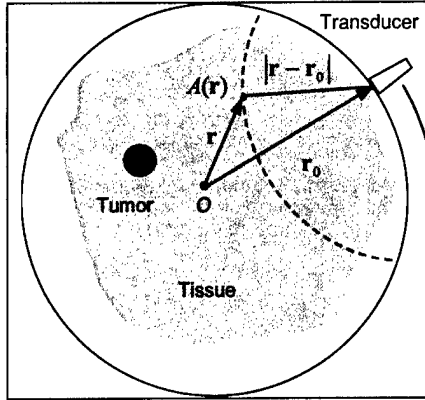


Fig. 1. Acoustic detection scheme. The ultrasonic transducer at position  $\mathbf{r}_0$  records the thermoacoustic signals on a spherical surface with radius  $|\mathbf{r} - \mathbf{r}_0|$ .

The above equation shows that the absorption distribution can be calculated by means of backprojection of the quantity  $-\frac{1}{t} \frac{\partial p(\mathbf{r}_0, t)}{\partial t} \Big|_{t=\frac{|\mathbf{r}_0-\mathbf{r}|}{c}}$  instead of the acoustic pressure itself. This

approximate algorithm involves less computing time than the exact inverse solution.

For initial investigations, we reconstruct individual cross sections of samples. In these cases, the backprojection is carried out in a circle around the cross sections, and the approximate inverse solution can be simplified as

$$A(\mathbf{r}) = -\frac{r_0^2}{\pi \eta c^4} \int_{\phi_0} d\phi_0 \frac{1}{t} \frac{\partial p(\mathbf{r}_0, t)}{\partial t} \Big|_{t=\frac{|\mathbf{r}_0-\mathbf{r}|}{c}}. \quad (18)$$

### Experimental method of thermoacoustic tomography

#### Experimental setup

**Fig. 2** shows the experimental setup. A plexiglass container is filled with mineral oil. A rotation stage and an unfocused ultrasonic transducer are immersed inside it in the same  $x$ - $y$  plane. The slice sample can be put in the rotation stage horizontally. The transducer points horizontally to the rotation center and detects the acoustic signal from the sample. A step motor directly drives the rotation stage while the transducer is fixed. Obviously, this is equivalent to having a transducer rotationally scanning the sample. The transducer (V323, Panametrics) has a central frequency of 2.25 MHz and a diameter of 6 mm.

The microwave pulses are transmitted from a 3-GHz microwave generator with a energy of 10 mJ/pulse and a pulse width of 0.5  $\mu$ s. A function generator (Protek, B-180) is used to trigger the microwave generator, control its pulse repetition frequency, and synchronize the oscilloscope sampling. Microwave energy is delivered to the sample from below by a rectangular waveguide with a cross section of 72 mm  $\times$  34 mm.

A personal computer is used to control the step motor in rotating the sample. The signal from the transducer is first amplified through a pulse amplifier, then recorded and averaged 200 times by an oscilloscope (TDS640A, Tektronix), and finally transferred to a personal computer for imaging.

Lastly, we want to point out that, in our experiments, the distance  $r_0$  between the rotation center and the surface of the transducer is 4.3 cm. In the frequency domain (60 KHz–1.8 MHz),  $|k|r_0 = 2\pi f r_0 / c$  with 1.5 mm/ $\mu$ s, we get  $10 < |k|r_0 < 330$ . Therefore, the required condition  $|k|r_0 \gg 1$  for the modified backprojection algorithm is satisfied.

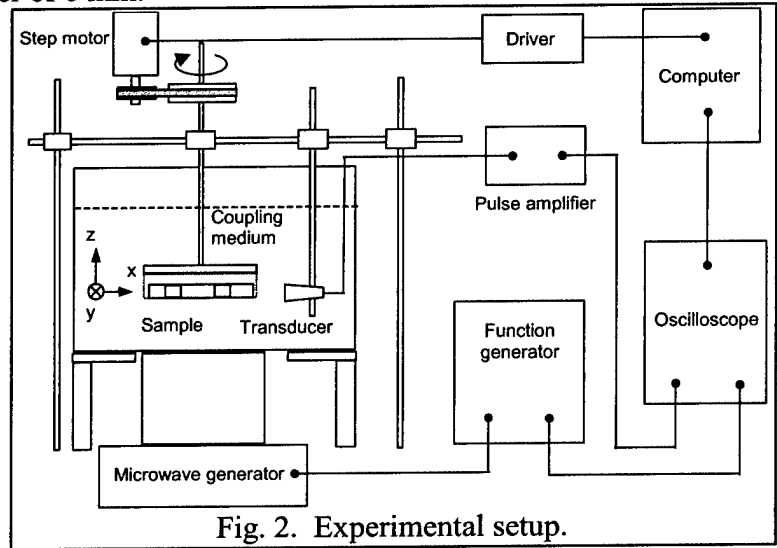


**Fig. 2.** Experimental setup.



### Technical consideration

The ultrasonic transducer is not a real point detector. For simplicity, we can ignore its size if we put it far away from the sample. However, we still have to consider the impulse response  $R(t)$  of the transducer and the pumping duration  $I(t)$  of the microwave pulse. In general, the measured piezoelectric signal can be written as a convolution:

$$S(\mathbf{r}_0, t) = p(\mathbf{r}_0, t) * I(t) * R(t), \quad (19)$$

where  $p(\mathbf{r}_0, t)$  is the thermoacoustic signal with delta-pulse microwave pumping. In the frequency domain, the above equation can be written as

$$S(\mathbf{r}_0, \omega) = p(\mathbf{r}_0, \omega) I(\omega) R(\omega), \quad (20)$$

where

$$I(\omega) = \int_{-\infty}^{+\infty} I(t) \exp(i\omega t) dt, \quad (21)$$

$$R(\omega) = \int_{-\infty}^{+\infty} R(t) \exp(i\omega t) dt. \quad (22)$$

Therefore,  $\frac{\partial p(\mathbf{r}_0, t)}{\partial t}$  can be calculated by an inverse Fourier transformation,

$$\begin{aligned} \frac{\partial p(\mathbf{r}_0, t)}{\partial t} &= \text{FFT}^{-1} \left\{ \frac{-i\omega S(\mathbf{r}_0, \omega)}{I(\omega) R(\omega)} F(\omega) \right\} \\ &= \frac{1}{2\pi} \int_{-\infty}^{+\infty} \frac{-i\omega S(\mathbf{r}_0, \omega)}{I(\omega) R(\omega)} F(\omega) \exp(-i\omega t) dt \end{aligned} \quad (23)$$

where  $F(\omega)$  is a wide band-pass filter, which is used to eliminate the noise at high frequencies as well as the low frequency component to guarantee the condition  $|k|r_0 \gg 1$  for the modified backprojection.

In our experiments,  $I(t)$  is approximately a rectangular function with duration  $\tau = 0.5 \mu\text{s}$ .

The ultrasonic transducer is of the videoscanner type with a central frequency  $f_0 = 2.25 \text{ MHz}$ . The generated thermoacoustic signal mainly exists in a frequency range below 1.8 MHz. Therefore, a band-pass filter  $F(\omega)$  may be employed in data processing, which lets only the signal in the range between 60 KHz and 1.8 MHz pass through.

### Results and discussion of thermoacoustic tomography

#### Image contrast

Image contrast is an important index for biological imaging. Fig. 3(a) shows a tested sample, which was photographed after the experiment. The sample was made according to the following procedure. First, we cut a thin piece of homogeneous pork fat tissue and shaped it arbitrarily to form a base. Its thickness is 5 mm and its maximum diameter is 4 cm. Then we used different screwdrivers to carefully make two pairs of holes that were approximately 4 mm and 6 mm in diameter, respectively. Finally, one big and one small hole on the left side was filled with pork

muscle, while the big and small hole on the right side were filled with pork fat of the same type as that which made up the base.

In the experiment, the transducer rotationally scanned the sample from 0 to 360 degrees with a step size of 2.25 degrees. We used the 160 series of data to calculate the image by our modified backprojection method.

The reconstructed image is shown in Fig. 3(b). The outline and size of the fat base as well as the sizes and locations of the two muscle pieces are in good agreement with the original sample in Fig. 3(a).

The high contrast is due to the low microwave absorption capacity of fat and the high absorption capacity of muscle: at 3 GHz, the penetration depth for muscle and fat are 1.2 cm and 9 cm, respectively. The two pieces of fat are not visible in the image Fig. 3(b), which means the minute mechanical discontinuity between the boundaries of muscle and fat does not contribute much to the thermoacoustic signal. On the contrary, the discontinuity improves the strength of the echo sounds in pure-ultrasound imaging.

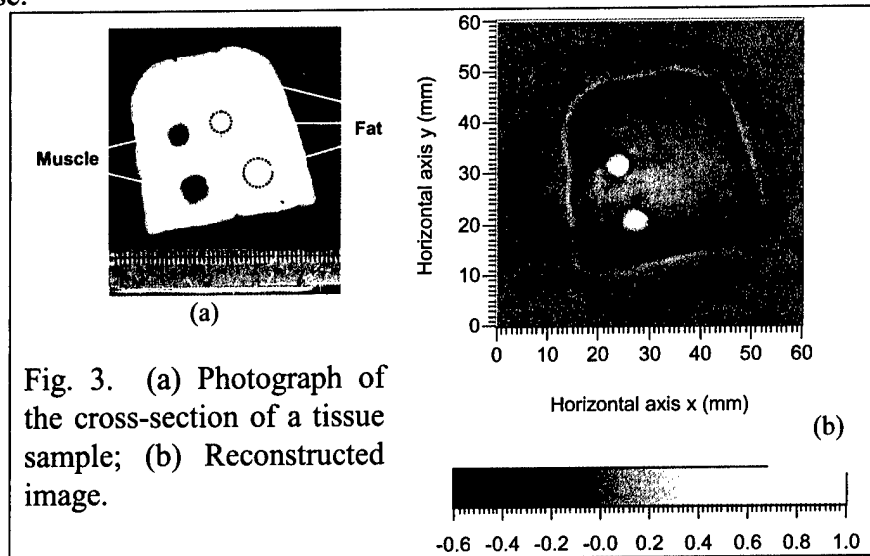


Fig. 3. (a) Photograph of the cross-section of a tissue sample; (b) Reconstructed image.

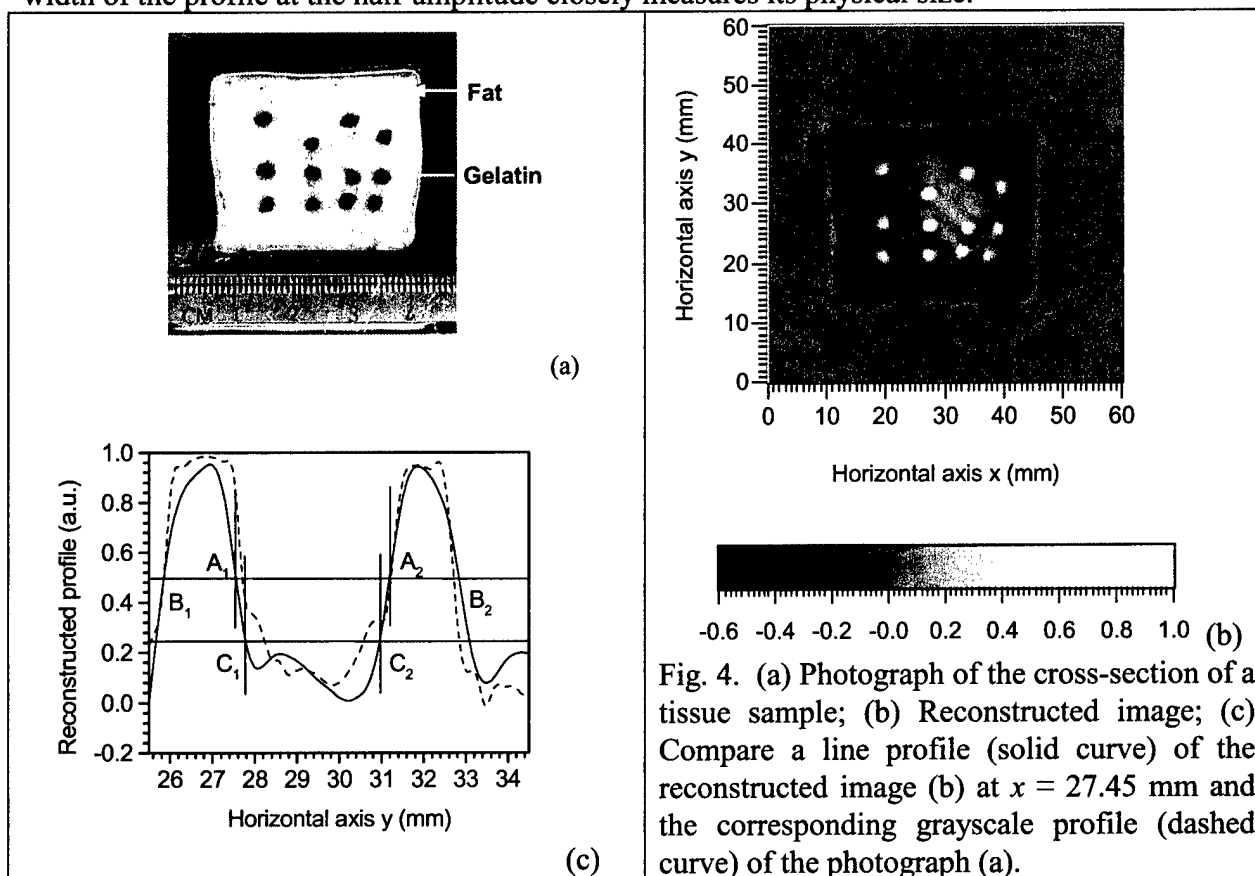
#### Spatial resolution

Spatial resolution is another important index for biological imaging. We used samples with a set of small thermoacoustic sources to test the resolution. One tested sample is shown in Fig. 4(a), which was also photographed after the experiment was completed.

The sample was made according to the following procedure. First, we cut a thin piece of homogeneous pork fat tissue and made it into an arbitrary shape. Its thickness was 5 mm with a maximum diameter of 4 cm. Then we used a small screwdriver to carefully make a set of small holes about 2 mm in diameter. In the meantime, we prepared a hot solution with 5% gelatin, 0.8% salt and a drop of dark ink (to improve the photographic properties of the sample). Next, we used an injector to inject a drop of the gelatin solution into each small hole and subsequently blew out the air to make good coupling between the gelatin solution and the fat tissue. After being cooled in room temperature for about 15 minutes, the gelatin solution was solidified. During the experiment, the transducer also rotationally scanned the sample from 0 to 360 degrees with a step size of 2.25 degrees.

The reconstructed image produced by our modified backprojection method is shown in Fig. 4(b), which agrees with the original sample very well. In particular, the relative locations and sizes of those small thermoacoustic sources are clearly resolved and perfectly match the original ones. Fig. 4(c) shows a reconstructed profile (solid curve) at position  $x = 27.45$  mm of the image Fig. 4(b), which includes two gelatin sources with a distance of about 3 mm. Each gelatin source has a distinct profile in the image. The boundaries between them are clearly

imaged. Moreover, the reconstructed profile is in good agreement with the original profile (dashed curve), which was a grayscale profile of the image Fig. 4(b). The half-amplitude line cuts across the reconstructed profile at points  $B_1$ ,  $A_1$ ,  $A_2$  and  $B_2$ , respectively. The distances  $|A_1B_1| = 1.72 \text{ mm}$  and  $|A_2B_2| = 1.67 \text{ mm}$  in the image are close to the original values of about 1.80 mm and 1.60 mm, respectively, which were measured in the original objects. Therefore, the width of the profile at the half-amplitude closely measures its physical size.



We here define a resolving criterion for estimating spatial resolution. The quarter-amplitude line cuts across the profiles at points  $C_1$  and  $C_2$ , respectively, as shown in Fig. 4(c). If the right source moves to the position of the left one, the reconstructed profile is equal to the spatial summation of the profiles of the two sources, because of the linear superposition property of acoustic waves. When point  $C_2$  encounters  $C_1$ , the new amplitude at  $C_2$  or  $C_1$  reaches half amplitude, and the two sources can still be differentiated. If the right one moves more to the left, the new amplitude between their overlap regions goes up more than half amplitude. When we use a half-amplitude line to cut across the profiles, we get only two points on the far side of each profile, which means that these two sources can no longer be clearly distinguished. Further, when point  $A_1$  touches  $A_2$ , these two sources join as an object.

Therefore, the minimum distance that can be differentiated is approximately equal to the summation of the horizontal distance between point  $A_1$  and  $C_1$  and the horizontal distance between point  $A_2$  and  $C_2$ . We have checked additional pairs of sources resembling those in the image of Fig. 4(b), and found that this minimum distance is less than 0.5 mm. We can, therefore,

claim the spatial resolution in our experiments reaches less than 0.5 mm, which agrees with the theoretical spatial resolution limit for 1.8 MHz signals whose half wavelength is  $\sim 0.5$  mm with the sound speed of 1.5 mm/ $\mu$ s.

Of course, the detecting transducer has a finite physical size. If it is close to the thermoacoustic sources, it cannot be approximated as a point detector. Its size will blur the images and decrease the spatial resolution. Therefore, in experiments, the transducer must be placed some distance away from the tissue samples. In general, due to the finite size of the transducer, the farther away the transducer is from the detection center, the better the resolution at the expense of the signal.

Other factors limiting spatial resolution are the duration of the microwave pulse and the impulse response of the transducer. In general, using a shorter microwave pulse will produce more high-frequency components in the thermoacoustic signals. Selection of the duration of the pulse is dependent on the experimental conditions and measurement systems.

### Images of thick samples

The diagram and the photograph of a thick sample are shown in Fig. 5(a) and (b), respectively. The reconstructed image produced by our modified backprojection method is shown in Fig. 5(c), which agrees with the original sample very well. The relative locations and sizes of those thermoacoustic sources perfectly match the buried objects in the original sample.

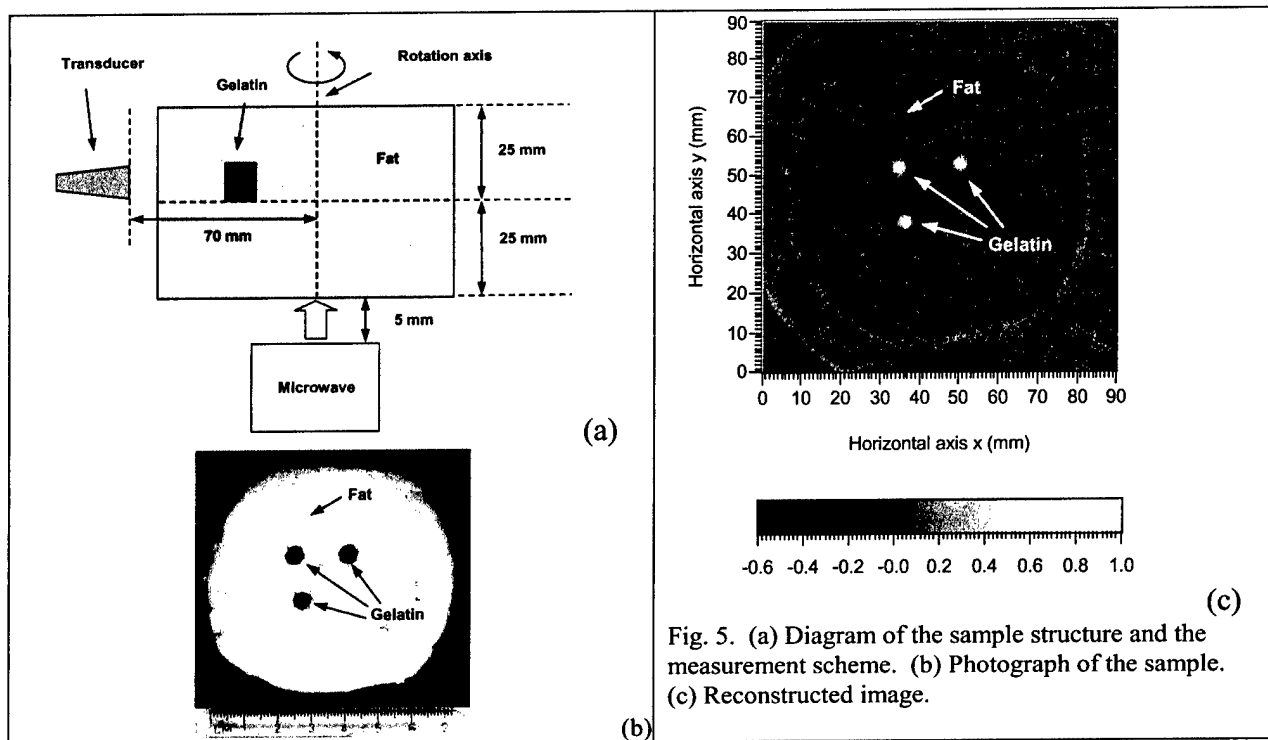


Fig. 5. (a) Diagram of the sample structure and the measurement scheme. (b) Photograph of the sample. (c) Reconstructed image.

### Statement of Work

Task 1: Setting up the scanning microwave-induced-acoustic tomography (SMIAT) instrument, Months 1–12:

- a. Modify/connect the microwave generator and the ultrasonic scanner.
- b. Image biological tissues in vitro with SMIAT.

Task 2. Extensive evaluation and optimization of the SMIAT setup, Months 13-36:

- a. Simulate microwave-induced-acoustic signals to provide guidance on the experiments.
- b. Optimize the ultrasonic and microwave parameters for good resolution and signal-to-noise ratio.
- c. Quantify the maximum imaging depth with SMIAT.
- d. Image biological tissues in vitro with SMIAT and quantify the imaging resolution.
- e. Image biological tissues in vitro with SMIAT and ultrasonography and quantify the contrast improvement of SMIAT over ultrasonography.
- f. Co-register the SMIAT images with the conventional ultrasonograms.

Task 1 has been successfully accomplished and Task 2 is ongoing as planned. We are well prepared to continue the project.

### **Key Research Accomplishments**

- An exact and an approximate time-domain reconstruction algorithm for thermoacoustic tomography in a spherical geometry was derived and published.
- An exact frequency-domain reconstruction algorithm for thermoacoustic tomography in a planar geometry was derived and published.
- An exact frequency-domain reconstruction algorithm for thermoacoustic tomography in a cylindrical geometry was derived and published.
- High-resolution and high-contrast images were obtained and published.

### **Reportable Outcomes**

#### Peer-reviewed journal articles

1. M. Xu and L.-H. Wang, "Time-domain reconstruction for thermoacoustic tomography in a spherical geometry," IEEE Transactions on Medical Imaging 21 (7), 814–822 (July 2002).
2. Y. Xu, D. Feng, and L.-H. Wang, "Exact frequency-domain reconstruction for thermoacoustic tomography—I: Planar geometry," IEEE Transactions on Medical Imaging 21 (7), 823–828 (July 2002).
3. Y. Xu, M. Xu, and L.-H. Wang, "Exact frequency-domain reconstruction for thermoacoustic tomography—II: Cylindrical geometry," IEEE Transactions on Medical Imaging 21 (7), 829–833 (July 2002).

#### Conference presentations/proceedings

1. M. Xu, X. Wang and L.-H. Wang, "RF- and laser-induced thermoacoustic tomography," pp. 406–408, *Advances in Optical Imaging and Photon Migration*, Optical Society of America, Miami Beach, Florida, April 7–10, 2002.

#### Invited talks

1. 02/27/2002, Ultrasound-mediated biophotonic imaging. Laser Diagnostic Technologies, Inc., San Diego, California.
2. 03/13/2002, Non-invasive skin detection by oblique-incidence reflectometry. STARTech Early Ventures, Richardson, Texas.
3. 04/26/2002, guest speaker for War On Cancer, 7<sup>th</sup> Annual Relay for Life, American Cancer Society, College Station, Texas. The other guest speakers are Texas A&M University System Chancellor Howard Graves and his wife, Mrs. Gracie Graves.
4. 05/13/2002, Biophotonic imaging: contrast, resolution, and ultrasonic mediation. Photonify Technologies Inc., Fremont, California.
5. 06/02/2002, Ultrasound-mediated biophotonic imaging. Workshop on Microwave Photonics for Medical Imaging, International Microwave Symposium, Seattle, Washington.
6. 06/02/2002, Biophotonic imaging: contrast, resolution, and ultrasonic mediation. Center for Industrial and Medical Ultrasound, University of Washington, Seattle, Washington.
7. 06/11/2002, Biophotonic imaging: contrast, resolution, and ultrasonic mediation. Department of Chemistry, University of California, Davis, California.
8. 06/23/2002, Ultrasound-mediated biophotonic imaging. International Quantum Electronics Conference (IQEC) and the Conference on Lasers, Applications, and Technologies (LAT), Presidium Building of the Russian Academy of Sciences (RAS), Moscow, Russia.
9. 06/27/2002, Biophotonic imaging: contrast, resolution, and ultrasonic mediation. ESPCI, Paris, France.

#### Degrees

1. None.

### Conclusions

Since October 2001, we have published three peer-reviewed journal articles in IEEE Transactions on Medical Imaging—a top imaging journal, published one conference proceedings article, and delivered 9 invited talks. This research has been exciting. We are well prepared to continue the project with greater successes.

The combination of ultrasound and microwave has provided us a unique opportunity for early-cancer imaging with high resolution and high contrast. We have made significant technical progress in thermoacoustic imaging including data acquisition and imaging reconstruction. Specifically, our accomplishments include (1) an exact and an approximate time-domain reconstruction algorithm for thermoacoustic tomography in a spherical geometry was derived and published, (2) an exact frequency-domain reconstruction algorithm for thermoacoustic tomography in a planar geometry was derived and published, (3) an exact frequency-domain reconstruction algorithm for thermoacoustic tomography in a cylindrical geometry was derived and published, and (4) high-resolution and high-contrast images were obtained and published. The reconstruction is an inverse source problem similar to that in PET (positron emission tomography); however, the reconstruction in PET is based on geometric optics whereas the reconstruction in thermoacoustic imaging is based on diffractive/wave optics. We have successfully imaged biological tissue with high resolution and high contrast. We will advance this technology toward clinical applications.

### References

1. M. Xu and L.-H. Wang, "Time-domain reconstruction for thermoacoustic tomography in a spherical geometry," *IEEE Transactions on Medical Imaging* 21 (7), 814–822 (July 2002).
2. Y. Xu, D. Feng, and L.-H. Wang, "Exact frequency-domain reconstruction for thermoacoustic tomography—I: Planar geometry," *IEEE Transactions on Medical Imaging* 21 (7), 823–828 (July 2002).
3. Y. Xu, M. Xu, and L.-H. Wang, "Exact frequency-domain reconstruction for thermoacoustic tomography—II: Cylindrical geometry," *IEEE Transactions on Medical Imaging* 21 (7), 829–833 (July 2002).
4. M. Xu, X. Wang and L.-H. Wang, "RF- and laser-induced thermoacoustic tomography," pp. 406–408, *Advances in Optical Imaging and Photon Migration*, Optical Society of America, Miami Beach, Florida, April 7–10, 2002.

## **Appendices (23 pages)**

### **Appendix 1 (9 pages)**

M. Xu and L.-H. Wang, "Time-domain reconstruction for thermoacoustic tomography in a spherical geometry," IEEE Transactions on Medical Imaging 21 (7), 814–822 (July 2002).

### **Appendix 2 (6 pages)**

Y. Xu, D. Feng, and L.-H. Wang, "Exact frequency-domain reconstruction for thermoacoustic tomography—I: Planar geometry," IEEE Transactions on Medical Imaging 21 (7), 823–828 (July 2002).

### **Appendix 3 (5 pages)**

Y. Xu, M. Xu, and L.-H. Wang, "Exact frequency-domain reconstruction for thermoacoustic tomography—II: Cylindrical geometry," IEEE Transactions on Medical Imaging 21 (7), 829–833 (July 2002).

### **Appendix 4 (3 pages)**

M. Xu, X. Wang and L.-H. Wang, "RF- and laser-induced thermoacoustic tomography," pp. 406–408, Advances in Optical Imaging and Photon Migration, Optical Society of America, Miami Beach, Florida, April 7–10, 2002.



# Time-Domain Reconstruction for Thermoacoustic Tomography in a Spherical Geometry

Minghua Xu and Lihong V. Wang\*

**Abstract**—Reconstruction-based microwave-induced thermoacoustic tomography in a spherical configuration is presented. Thermoacoustic waves from biological tissue samples excited by microwave pulses are measured by a wide-band unfocused ultrasonic transducer, which is set on a spherical surface enclosing the sample. Sufficient data are acquired from different directions to reconstruct the microwave absorption distribution. An exact reconstruction solution is derived and approximated to a modified backprojection algorithm. Experiments demonstrate that the reconstructed images agree well with the original samples. The spatial resolution of the system reaches 0.5 mm.

**Index Terms**—Microwave, reconstruction, thermoacoustic, tomography.

## I. INTRODUCTION

**P**ULSED-MICROWAVE-INDUCED thermoacoustic tomography in biological tissues combines the advantages of pure microwave imaging [1]–[3] and pure ultrasound imaging [4], [5]. The wide range of microwave absorption coefficients found in different kinds of tissue leads to a high imaging contrast for biological tissues. However, it is difficult to achieve good spatial resolution in biological tissues using pure microwave imaging because of the long wavelength of microwaves. This problem can be overcome by the use of microwave-induced thermoacoustic waves. Because the velocity of acoustic waves in soft tissue is  $\sim 1.5 \text{ mm}/\mu\text{s}$ , thermoacoustic signals at megahertz can provide millimeter or better spatial resolution.

In thermoacoustic tomography, a short-pulsed microwave source is used to irradiate the tissue. The relatively long wavelength of the microwave, e.g.,  $\sim 3 \text{ cm}$  at 3 GHz in tissues, serves to illuminate the tissue homogeneously. A wide-band ultrasonic transducer can then be employed to acquire the thermoacoustic signals excited by thermoelastic expansion, which carries the microwave absorption property of the tissue.

Manuscript received May 15, 2001; revised May 13, 2002. This work was supported in part by the U.S. Army under Medical Research and Material Command under Grant DAMD17-00-1-0455, in part by the National Institutes of Health (NIH) under Grant R01 CA71980, in part by the National Science Foundation (NSF) under Grant BES-9734491, and in part by the Texas Higher Education Coordinating Board under Grant ARP000512-0123-1999. The Associate Editor responsible for coordinating the review of this paper and recommending its publication was G. Wang. *Asterisk indicates corresponding author.*

M. Xu is with the Optical Imaging Laboratory, Department of Biomedical Engineering, Texas A&M University, 3120 TAMU, College Station, TX 77843-3120 USA.

\*L. V. Wang is with the Optical Imaging Laboratory, Department of Biomedical Engineering, Texas A&M University, College Station, TX 77843-3120 USA (e-mail: LWang@tamu.edu).

Publisher Item Identifier 10.1109/TMI.2002.801176.

The ultrasonic transducer is very sensitive in detecting small thermoacoustic vibrations from an object.

The key problem with this technique is how to determine the microwave absorption distribution from the measured data, i.e., how to map the inhomogeneity of the tissue. One approach is to use focused ultrasonic transducers to localize the thermoacoustic sources in linear or sector scans and then construct the images directly from the data as is often done in pulse-echo ultrasonography [6], [7]. An alternative method is to use wide-band point detectors to acquire thermoacoustic data and then reconstruct the microwave absorption distribution. To date, we have not seen an exact inverse solution for this specific problem, although some researchers have arrived at approximate reconstruction algorithms, such as the weighted delay-and-sum method [8], the optimal statistical approach [9], and other approach [10].

Based on spherical harmonic functions, in this paper we first deduce an exact solution to the problem in three-dimensional spherical geometry, which can be carried out in the frequency domain [11]–[14]. The exact reconstruction algorithms in planar and cylindrical geometries are reported in the companion papers [15], [16]. Spherical measurement geometry may be more suitable for investigation of external organs such as the breast. We assume that the wide-band unfocused ultrasonic transducer is set on a spherical surface, which encloses the sample under investigation. The data acquired from different directions are sufficient to allow us to reconstruct the microwave absorption distribution.

In many cases, the diameter of the sphere of detection is much larger than the ultrasonic wavelength. As a result, an approximate algorithm can be deduced, which is a modified backprojection of a quantity related to the thermoacoustic pressure. This approximate algorithm can be carried out in the time domain and is much faster than the exact solution. In our initial investigations, we have also tested tissue samples in a circular measurement configuration. These experiments demonstrate that the images calculated by the modified backprojection method agree well with the original samples. Moreover, the images have both the high contrast associated with pure microwave imaging and the 0.5-mm spatial resolution associated with pure ultrasonic imaging.

## II. THEORY

### A. Fundamental of Thermoacoustics

Thermoacoustic theory has been discussed in many literature reviews such as [13]. Here, we briefly review only the fundamental equations. If the microwave pumping pulse duration is

much shorter than the thermal diffusion time, thermal diffusion can be neglected; consequently, the thermal equation becomes

$$\rho C_p \frac{\partial}{\partial t} T(\mathbf{r}, t) = H(\mathbf{r}, t) \quad (1)$$

where  $\rho$  is the density;  $C_p$  is the specific heat;  $T(\mathbf{r}, t)$  is the temperature rise due to the energy pumping pulse; and  $H(\mathbf{r}, t)$  is the heating function defined as the thermal energy per time and volume deposited by the energy source. We are initially interested in tissue with inhomogeneous microwave absorption but a relatively homogeneous acoustic property. The two basic acoustic generation equations in an acoustically homogeneous medium are the linear inviscid force equation

$$\rho \frac{\partial^2}{\partial t^2} \mathbf{u}(\mathbf{r}, t) = -\nabla p(\mathbf{r}, t) \quad (2)$$

and the expansion equation

$$\nabla \cdot \mathbf{u}(\mathbf{r}, t) = -\frac{p(\mathbf{r}, t)}{\rho c^2} + \beta T(\mathbf{r}, t) \quad (3)$$

where  $\beta$  is the isobaric volume expansion coefficient;  $c$  is the sound speed;  $\mathbf{u}(\mathbf{r}, t)$  is the acoustic displacement; and  $p(\mathbf{r}, t)$  is the acoustic pressure.

Combining (1)–(3), the pressure  $p(\mathbf{r}, t)$  produced by the heat source  $H(\mathbf{r}, t)$  obeys the following equation:

$$\nabla^2 p(\mathbf{r}, t) - \frac{1}{c^2} \frac{\partial^2}{\partial t^2} p(\mathbf{r}, t) = -\frac{\beta}{C_p} \frac{\partial}{\partial t} H(\mathbf{r}, t). \quad (4)$$

The solution based on Green's function can be found in the literature of physics or mathematics [12], [14]. A general form can be expressed as

$$p(\mathbf{r}, t) = \frac{\beta}{4\pi C_p} \iiint \frac{d^3 \mathbf{r}'}{|\mathbf{r} - \mathbf{r}'|} \frac{\partial H(\mathbf{r}', t')}{\partial t'} \bigg|_{t' = t - (|\mathbf{r} - \mathbf{r}'|/c)} \quad (5)$$

The heating function can be written as the product of a spatial absorption function and a temporal illumination function

$$H(\mathbf{r}, t) = A(\mathbf{r})I(t). \quad (6)$$

Thus,  $p(\mathbf{r}, t)$  can be expressed as

$$p(\mathbf{r}, t) = \frac{\beta}{4\pi C_p} \iiint \frac{d^3 \mathbf{r}'}{|\mathbf{r} - \mathbf{r}'|} A(\mathbf{r}')I'(t') \quad (7)$$

where  $I'(t') = dI(t')/dt'$ .

### B. Exact Reconstruction Theory

We first solve the problem where the pulse pumping is a Dirac delta function

$$I(t) = \delta(t). \quad (8)$$

Suppose the detection point on the spherical surface  $\mathbf{r} = \mathbf{r}_0$ , which encloses the sample (Fig. 1). By dropping the primes, (7) may be rewritten as

$$p(\mathbf{r}_0, t) = \eta \iiint d^3 \mathbf{r} A(\mathbf{r}) \frac{\delta'(t - \frac{|\mathbf{r}_0 - \mathbf{r}|}{c})}{4\pi |\mathbf{r}_0 - \mathbf{r}|} \quad (9)$$

where  $\eta = \beta/C_p$ . The inverse problem is to reconstruct the absorption distribution  $A(\mathbf{r})$  from a set of data  $p(\mathbf{r}_0, t)$  measured at positions  $\mathbf{r}_0$ . Taking the Fourier transform on variable  $t$  of (9), and denoting  $k = \omega/c$ , we get

$$\tilde{p}(\mathbf{r}_0, \omega) = -i\omega\eta \iiint d^3 \mathbf{r} A(\mathbf{r}) \frac{\exp(ik|\mathbf{r}_0 - \mathbf{r}|)}{4\pi |\mathbf{r}_0 - \mathbf{r}|} \quad (10)$$

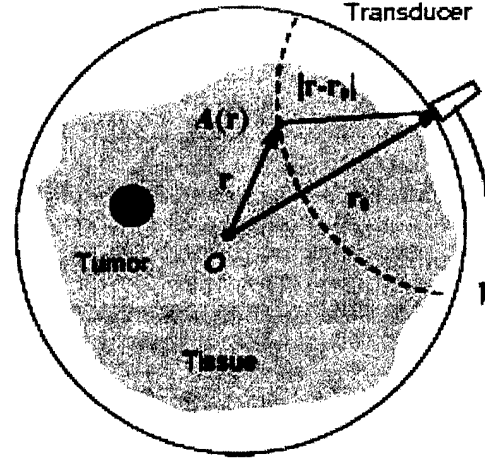


Fig. 1. Acoustic detection scheme. The ultrasonic transducer at position  $\mathbf{r}_0$  records the thermoacoustic signals on a spherical surface with radius  $|\mathbf{r} - \mathbf{r}_0|$ .

where the following Fourier transform pair exists:

$$\tilde{p}(\mathbf{r}_0, \omega) = \int_{-\infty}^{+\infty} p(\mathbf{r}_0, t) \exp(i\omega t) dt, \quad (11a)$$

$$p(\mathbf{r}_0, t) = \frac{1}{2\pi} \int_{-\infty}^{+\infty} \tilde{p}(\mathbf{r}_0, \omega) \exp(-i\omega t) d\omega. \quad (11b)$$

We next derive the exact solution using the spherical harmonic function basis. In the derivation, we referred to the mathematical techniques for ultrasonic reflectivity imaging [11]. The mathematics utilized can also be found routinely in the mathematical literature, such as [12]. Here, we list the identities (12a)–(12f) used in the subsequent deduction:

- 1) The complete orthogonal integral of spherical harmonics  $Y_l^m(\theta_0, \varphi_0)$

$$\iint_{\Omega_0} Y_l^m(\theta_0, \varphi_0) Y_k^{n*}(\theta_0, \varphi_0) d\Omega_0 = \delta_{l,k} \delta_{m,n} \quad (12a)$$

where  $d\Omega_0 = \sin \theta_0 d\theta_0 d\varphi_0$  and  $*$  denotes the complex conjugate.

- 2) The Legendre polynomial

$$P_l(\mathbf{n} \cdot \mathbf{n}_0) = \frac{4\pi}{2l+1} \sum_{m=-l}^{+l} Y_l^m(\theta, \varphi) Y_l^{m*}(\theta_0, \varphi_0) \quad (12b)$$

where the unit vectors  $\mathbf{n}$  and  $\mathbf{n}_0$  point in the directions  $(\theta, \varphi)$  and  $(\theta_0, \varphi_0)$ , respectively.

- 3) The orthogonal integral of Legendre polynomials, derived from (12a) and (12b)

$$\iint_{\Omega_0} d\Omega_0 P_l(\mathbf{n} \cdot \mathbf{n}_0) P_m(\mathbf{n}' \cdot \mathbf{n}_0) = \frac{4\pi}{2l+1} \delta_{lm} P_l(\mathbf{n} \cdot \mathbf{n}') \quad (12c)$$

where the unit vector  $\mathbf{n}' = \mathbf{r}'/r'$  points in the direction  $(\theta', \varphi')$ .

- 4) The expansion identity

$$\frac{\exp(ik|\mathbf{r}_0 - \mathbf{r}|)}{4\pi |\mathbf{r}_0 - \mathbf{r}|} = \frac{ik}{4\pi} \sum_{l=0}^{\infty} (2l+1) j_l(kr) h_l^{(1)}(kr_0) P_l(\mathbf{n} \cdot \mathbf{n}_0), \quad (k > 0) \quad (12d)$$

where  $\mathbf{n} = \mathbf{r}/r$ ,  $\mathbf{n}_0 = \mathbf{r}_0/r_0$ ,  $j_l(\cdot)$  and  $h_l^{(1)}(\cdot)$  are the spherical Bessel and Hankel functions, respectively.

5) The complete orthogonal integral of Bessel functions

$$\int_0^{+\infty} dk k^2 j_m(kr) j_m(kr') = \frac{\pi}{2r^2} \delta(r - r'). \quad (12e)$$

6) The summation identity of Legendre polynomials

$$\sum_{m=0}^{\infty} (2m+1) P_m(\mathbf{n} \cdot \mathbf{n}') = \frac{4\pi \delta(\theta - \theta') \delta(\varphi - \varphi')}{\sin \theta}. \quad (12f)$$

First, substituting (12d) into (10), we obtain

$$\tilde{p}(\mathbf{r}_0, \omega) = \frac{\omega k \eta}{4\pi} \iiint d^3r A(\mathbf{r}) \sum_{l=0}^{\infty} (2l+1) j_l(kr) \cdot h_l^{(1)}(kr_0) P_l(\mathbf{n} \cdot \mathbf{n}_0). \quad (13)$$

Then, multiplying both sides of (13) by  $P_m(\mathbf{n}' \cdot \mathbf{n}_0)$ , and integrating with respect to  $\mathbf{n}_0$  over the surface of the sphere, and considering the identity (12c), we obtain

$$\begin{aligned} & \iint_{\Omega_0} d\Omega_0 \tilde{p}(\mathbf{r}_0, \omega) P_m(\mathbf{n}' \cdot \mathbf{n}_0) \\ &= \frac{\omega k \eta}{4\pi} \iiint d^3r A(\mathbf{r}) \sum_{l=0}^{\infty} (2l+1) j_l(kr) h_l^{(1)}(kr_0) \\ & \quad \cdot \iint_{\Omega_0} d\Omega_0 P_l(\mathbf{n} \cdot \mathbf{n}_0) P_m(\mathbf{n}' \cdot \mathbf{n}_0) \\ &= \frac{\omega k \eta}{4\pi} \iiint d^3r A(\mathbf{r}) \sum_{l=0}^{\infty} (2l+1) j_l(kr) h_l^{(1)}(kr_0) \frac{4\pi}{2l+1} \\ & \quad \cdot \delta_{lm} P_l(\mathbf{n} \cdot \mathbf{n}') \\ &= k^2 \eta c \iiint d^3r A(\mathbf{r}) j_m(kr) h_m^{(1)}(kr_0) P_m(\mathbf{n} \cdot \mathbf{n}') \end{aligned}$$

i.e.,

$$\begin{aligned} & \iint_{\Omega_0} d\Omega_0 \tilde{p}(\mathbf{r}_0, \omega) P_m(\mathbf{n}' \cdot \mathbf{n}_0) \frac{1}{h_m^{(1)}(kr_0)} \\ &= k^2 \eta c \iiint d^3r A(\mathbf{r}) j_m(kr) P_m(\mathbf{n} \cdot \mathbf{n}'). \quad (14) \end{aligned}$$

Further, multiplying both sides of (14) by  $j_m(kr')$ , integrating them with respect to  $k$  from zero to  $+\infty$ , and then multiplying both sides of (14) again by  $(2m+1)$  and summing  $m$  from zero to  $\infty$ , and considering the identity (12e) and (12f), we get

$$\begin{aligned} & \iint_{\Omega_0} d\Omega_0 \int_0^{+\infty} dk \tilde{p}(\mathbf{r}_0, \omega) \sum_{m=0}^{\infty} \frac{(2m+1) j_m(kr')}{h_m^{(1)}(kr_0)} P_m(\mathbf{n}' \cdot \mathbf{n}_0) \\ &= \eta c \iiint d^3r A(\mathbf{r}) \sum_{m=0}^{\infty} (2m+1) P_m(\mathbf{n} \cdot \mathbf{n}') \int_0^{+\infty} dk k^2 \\ & \quad \cdot j_m(kr') j_m(kr) \\ &= \eta c \iiint d^3r A(\mathbf{r}) \frac{4\pi \delta(\theta - \theta') \delta(\varphi - \varphi')}{\sin \theta} \frac{\pi}{2r^2} \delta(r - r') \\ &= 2\pi^2 \eta c A(\mathbf{r}'). \end{aligned}$$

Finally, dropping the primes, we can rewrite the equation as

$$\begin{aligned} A(\mathbf{r}) &= \frac{1}{2\pi^2 \eta c} \iint_{\Omega_0} d\Omega_0 \int_0^{+\infty} dk \tilde{p}(\mathbf{r}_0, \omega) \\ & \quad \cdot \sum_{m=0}^{\infty} \frac{(2m+1) j_m(kr)}{h_m^{(1)}(kr_0)} P_m(\mathbf{n} \cdot \mathbf{n}_0). \quad (15) \end{aligned}$$

This is the exact inverse solution of (9). It involves summation of a series and may take much time to compute. Therefore, it is desirable to further simplify the solution.

### C. Modified Backprojection

In experiments, the detection radius  $r_0$  is usually much larger than the wavelengths of the thermoacoustic waves that are useful for imaging. Because the low-frequency component of the thermoacoustic signal does not significantly contribute to the spatial resolution, it can be removed by a filter. Therefore, we can assume  $|k|r_0 \gg 1$  and use the asymptotic form of the Hankel function to simplify (15). The following two identities are involved [12]:

1) The expansion identity similar to (12d)

$$\frac{\exp(-ik|\mathbf{r}_0 - \mathbf{r}|)}{4\pi|\mathbf{r}_0 - \mathbf{r}|} = \frac{-ik}{4\pi} \sum_{m=0}^{\infty} (2m+1) j_m(kr) \cdot h_m^{(2)}(kr_0) P_m(\mathbf{n} \cdot \mathbf{n}_0), \quad (k > 0). \quad (16a)$$

2) The approximation when  $|k|r_0 \gg 1$

$$h_m^{(1)}(kr_0) \approx \frac{1}{h_m^{(2)}(kr_0)} \left( \frac{1}{(kr_0)^2} + O\left(\frac{1}{(kr_0)^4}\right) \right) \quad (16b)$$

where  $h_l^{(2)}(\cdot)$  is the spherical Hankel function of the second kind.

Substituting (16b) into (15), we get

$$\begin{aligned} A(\mathbf{r}) &\approx \frac{1}{2\pi^2 \eta c} \iint_{\Omega_0} d\Omega_0 \int_0^{+\infty} dk \tilde{p}(\mathbf{r}_0, \omega) k^2 r_0^2 \sum_{m=0}^{\infty} (2m+1) \\ & \quad \cdot j_m(kr) h_m^{(2)}(kr_0) P_m(\mathbf{n} \cdot \mathbf{n}_0). \quad (17) \end{aligned}$$

Considering the form of (16a), the above equation can be rewritten as

$$\begin{aligned} A(\mathbf{r}) &= \frac{r_0^2}{2\pi^2 \eta c} \iint_{\Omega_0} d\Omega_0 \int_0^{+\infty} dk \tilde{p}(\mathbf{r}_0, \omega) (ik) \\ & \quad \cdot \frac{\exp(-ik|\mathbf{r}_0 - \mathbf{r}|)}{|\mathbf{r}_0 - \mathbf{r}|} \\ &= -\frac{r_0^2}{\pi \eta c^3} \iint_{\Omega_0} d\Omega_0 \frac{1}{2\pi} \int_0^{+\infty} d\omega \tilde{p}(\mathbf{r}_0, \omega) (-i\omega) \\ & \quad \cdot \frac{\exp\left(-i\omega \frac{|\mathbf{r}_0 - \mathbf{r}|}{c}\right)}{|\mathbf{r}_0 - \mathbf{r}|}. \end{aligned}$$

Because  $p(\mathbf{r}, t)$  is a real function,  $p^*(\mathbf{r}, \omega) = p(\mathbf{r}, -\omega)$ . Taking the summation of the above equation with its complex conjugate and then dividing it by two, we get

$$\begin{aligned} A(\mathbf{r}) &= \frac{r_0^2}{4\pi^2 \eta c} \iint_{\Omega_0} d\Omega_0 \int_{-\infty}^{+\infty} dk \tilde{p}(\mathbf{r}_0, \omega) (ik) \\ & \quad \cdot \frac{\exp(-ik|\mathbf{r}_0 - \mathbf{r}|)}{|\mathbf{r}_0 - \mathbf{r}|} \\ &= -\frac{r_0^2}{2\pi \eta c^3} \iint_{\Omega_0} d\Omega_0 \frac{1}{2\pi} \int_{-\infty}^{+\infty} d\omega \tilde{p}(\mathbf{r}_0, \omega) (-i\omega) \\ & \quad \cdot \frac{\exp\left(-i\omega \frac{|\mathbf{r}_0 - \mathbf{r}|}{c}\right)}{|\mathbf{r}_0 - \mathbf{r}|}. \end{aligned}$$

Recalling the inverse Fourier transform (11b), we get

$$A(\mathbf{r}) = -\frac{r_0^2}{2\pi\eta c^3} \iint_{\Omega_0} d\Omega_0 \frac{1}{|\mathbf{r}_0 - \mathbf{r}|} \left. \frac{\partial p(\mathbf{r}_0, t)}{\partial t} \right|_{t=|\mathbf{r}_0 - \mathbf{r}|/c} \quad (18)$$

i.e.,

$$A(\mathbf{r}) = -\frac{r_0^2}{2\pi\eta c^4} \iint_{\Omega_0} d\Omega_0 \frac{1}{t} \left. \frac{\partial p(\mathbf{r}_0, t)}{\partial t} \right|_{t=|\mathbf{r}_0 - \mathbf{r}|/c}. \quad (19)$$

Equation (19) shows that the absorption distribution can be calculated in the time domain by the means of backprojection and coherent summation over spherical surfaces of the quantity  $-(1/t)(\partial p(\mathbf{r}_0, t)/\partial t)$  instead of the acoustic pressure itself. This approximate algorithm requires less computing time than the exact solution (15).

For initial investigations, we measure the samples in a circular configuration. In these cases, the backprojection is carried out in a circle around the slices, and (19) can be simplified to

$$A(\mathbf{r}) = -\frac{r_0^2}{2\pi\eta c^4} \int_{\varphi_0} d\varphi_0 \frac{1}{t} \left. \frac{\partial p(\mathbf{r}_0, t)}{\partial t} \right|_{t=|\mathbf{r}_0 - \mathbf{r}|/c}. \quad (20)$$

### III. EXPERIMENTAL METHOD

#### A. Diagram of Setup

Fig. 2 shows the experimental setup for the circular measurement configuration, which is modified from our previous paper [7]. For the convenience of the reader, the system is briefly described here. The unfocused transducer (V323, Panametrics) has a central frequency of 2.25 MHz and a diameter of 6 mm. It is fixed and it points horizontally to the center of the rotation stage, which is used to hold the samples. For good coupling of acoustic waves, both the transducer and the sample are immersed in mineral oil in a container.

The microwave pulses are transmitted from a 3-GHz microwave generator with a pulse energy of 10 mJ and a width of 0.5  $\mu$ s, and then delivered to the sample from the bottom by a rectangular waveguide with a cross section of 72 mm  $\times$  34 mm. A function generator (Protek, B-180) is used to trigger the microwave generator, control its pulse repetition frequency, and synchronize the oscilloscope sampling. The signal from the transducer is first amplified through a pulse amplifier, then recorded and averaged 200 times by an oscilloscope (TDS640A, Tektronix). A personal computer is used to control the step motor for rotating the sample and transferring the data.

Last, we want to point out that, in our experiments, the smallest distance  $r_0$  between the frequency center and the surface of the transducer is 4.3 cm. In the frequency domain (100 KHz–1.8 MHz),  $|k|r_0 = 2\pi r_0 f/c$  with 1.5 mm/ $\mu$ s, we get  $18 < |k|r_0 < 330$ . Therefore, the required condition  $|k|r_0 \gg 1$  for the modified backprojection algorithm is satisfied.

#### B. Technical Consideration

During measurement, we find that the piezoelectric signal  $S_0(\mathbf{r}_0, t)$  detected by the transducer includes the thermal acoustic signal  $S(\mathbf{r}_0, t)$  as well as some noise. The noise comes from two contributors. One is the background random noise of the measurement system, which can be suppressed by averaging the measured data. The other part,  $S_{mp}(t)$ , results from the microwave pumping via electromagnetic induction.

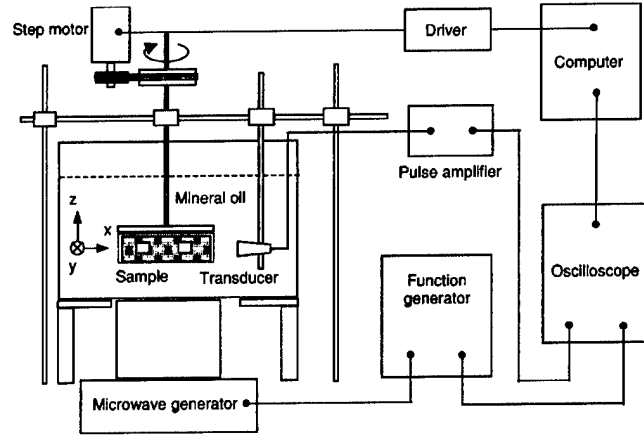


Fig. 2. The experimental setup.

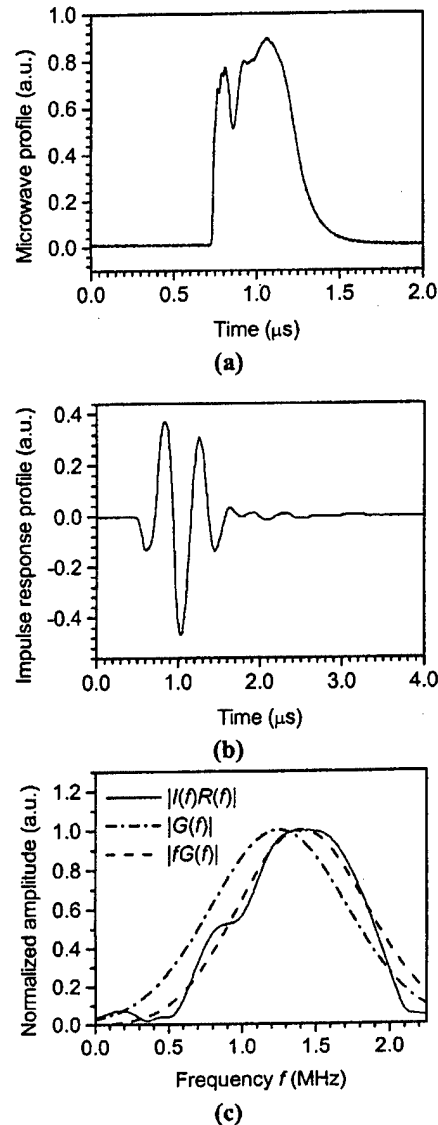


Fig. 3. (a) The temporal profile of the microwave pulse; (b) the temporal profile of the impulse response of the transducer; (c) compare the normalized amplitudes of the spectrum  $I(f)R(f)$ ,  $G(f)$  and  $fG(f)$ .

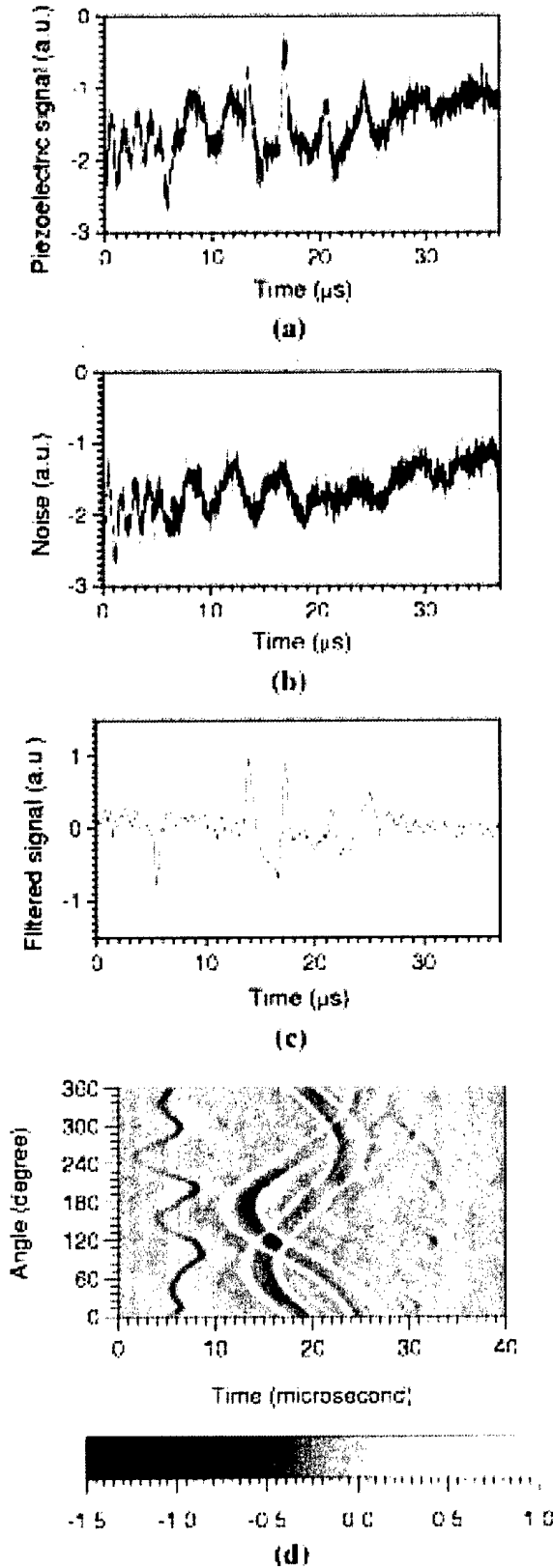


Fig. 4. (a) An example of temporal piezoelectric signal; (b) an example of temporal noise; (c) an example of filtered signal; and (d) an example of filtered thermoacoustic signals detected at different angular positions from  $0^\circ$  to  $360^\circ$ .

The pumping component of the noise can be measured without a sample, and can be subtracted from the measured data

$$S(\mathbf{r}_0, t) \approx S_0(\mathbf{r}_0, t) - S_{mp}(t). \quad (21)$$

In fact, the transducer is not a real point detector. For simplicity, we can ignore its size if we put it far away from the sample. However, we still have to consider the impulse response  $R(t)$  of the transducer and the pumping duration  $I(t)$  of the microwave pulse. In general, the measured thermoacoustic signal can be written as a convolution

$$S(\mathbf{r}_0, t) = p(\mathbf{r}_0, t) * I(t) * R(t) \quad (22)$$

where  $p(\mathbf{r}_0, t)$  is the thermoacoustic signal with delta-pulse microwave pumping. In the frequency domain, (22) can be written as

$$S(\mathbf{r}_0, \omega) = p(\mathbf{r}_0, \omega)I(\omega)R(\omega) \quad (23)$$

where

$$I(\omega) = \int_{-\infty}^{+\infty} I(t) \exp(i\omega t) dt, \quad (24a)$$

$$R(\omega) = \int_{-\infty}^{+\infty} R(t) \exp(i\omega t) dt. \quad (24b)$$

Because of the presence of noise and the finite bandwidth of  $I(\omega)$  and  $R(\omega)$ , an appropriate deconvolution algorithm should be used to calculate  $p(\mathbf{r}_0, \omega)$ . In the reconstruction, only the high-frequency component of the thermoacoustic signal is required. Therefore, we compute  $p(\mathbf{r}_0, \omega)G(\omega)$  instead, where  $G(\omega)$  is a high-frequency bandpass filter such as a Gaussian filter

$$G(\omega) = \exp \left[ -\alpha \left( \frac{\omega}{\omega_0} - 1 \right)^2 \right]$$

and  $\alpha$  and  $\omega_0$  are two parameters of the filter,  $\omega = 2\pi f$  and  $\omega_0 = 2\pi f_0$ .

In our experiments,  $I(t)$  is approximately a rectangular function with duration  $\tau = 0.5 \mu s$  and its temporal profile is shown in Fig. 3(a). Its spectrum  $I(\omega)$  covers the range from 0 to 2 MHz. The transducer that we used is of the videoscanner type with a central frequency of  $f_0 = 2.25$  MHz, and the temporal profile of the impulse response is shown in Fig. 3(b). It is observed that the generated thermoacoustic signal under microwave pumping with duration  $\tau = 0.5 \mu s$  exists primarily in a frequency range below 1.8 MHz. We chose the parameters  $\alpha = 3.6$  and  $f_0 = 1.25$  MHz in the Gaussian filter

$$G(f) = \exp \left[ -\alpha \left( \frac{f}{f_0} - 1 \right)^2 \right]$$

to eliminate the noise at high as well as low frequencies. The spectrum  $G(f)$  is shown as the dash-dot line in Fig. 3(c). We compared the normalized spectrum  $I(f)R(f)$  [solid line in Fig. 3(c)] with  $fG(f)$  [dash line in Fig. 3(c)], and found  $|fG(f)| \approx |I(f)R(f)|$  when  $f < 2$  MHz. Of course, this approximated equality is a special case for our measurement system only. Therefore, the filtered  $\partial p(\mathbf{r}_0, t)/\partial t$  can be simply calculated by an inverse fast Fourier transform (IFFT)

$$\frac{\partial p(\mathbf{r}_0, t)}{\partial t} \approx \text{IFFT} \{ S(\mathbf{r}_0, \omega)F(\omega) \} \quad (25)$$

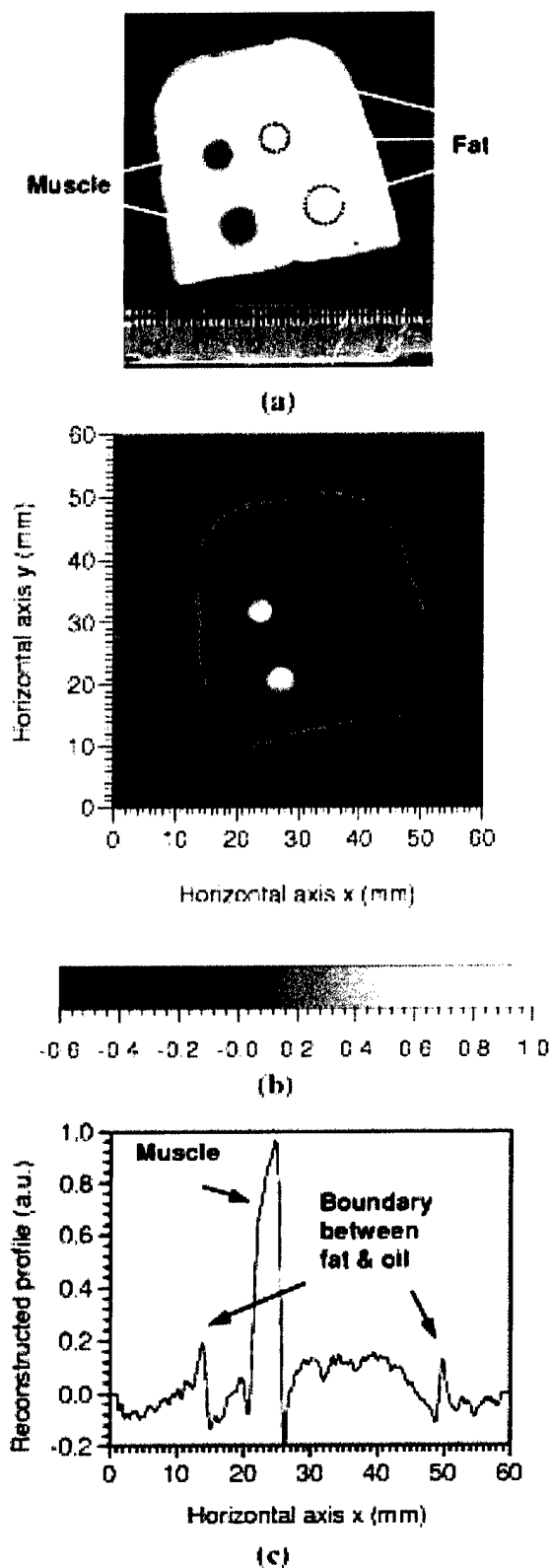


Fig. 5. (a) Cross section of a tissue sample; (b) reconstructed image; and (c) a line profile of the reconstructed image at  $y = 31.5$  mm.

where  $F(\omega)$  is a wide bandpass filter, which is used to further eliminate noise at high and low frequencies in order to guarantee

the condition  $|k|r_0 \gg 1$  for the modified backprojection. A simple filter is

$$F(f) = \begin{cases} 1, & 0.1 \text{ MHz} < f < 1.8 \text{ MHz} \\ 0, & \text{otherwise.} \end{cases} \quad (26)$$

#### IV. RESULTS AND DISCUSSION

Finally, we use the above modified backprojection algorithm and the experimental method to investigate some tissue samples.

##### A. Experimental Data Preprocessing

The measured piezoelectric data include the useful thermoacoustic signal as well as some noise data as illustrated by the following example. Fig. 4(a) is a typical measured temporal piezoelectric signal, which is from the sample shown in Fig. 5(a). One portion of the noise resulting from the microwave pumping looks like the curve in Fig. 4(b), which is acquired at the same sampling rate and the same delay time with the transducer in the same position as the curve in Fig. 4(a). Because the slice is very thin, the thermoacoustic signal is not much higher than the noise resulting from the microwave pumping. Next, we subtract the noise from the raw thermoacoustic signal and use a wide bandpass filter to eliminate some of the useless low-frequency and high-frequency components. This processed data is shown in Fig. 4(c); it is much cleaner than the raw data in Fig. 4(a). The filtered thermoacoustic signals detected at different angular positions from  $0^\circ$  to  $360^\circ$  are shown in Fig. 4(d).

##### B. Image Contrast

Image contrast is an important index for biological imaging. Fig. 5(a) shows a tested sample, which was photographed after the experiment. The sample was made according to the following procedure. First, we cut a thin piece of homogeneous pork fat tissue and shaped it arbitrarily to form a base. Its thickness is 5 mm and its maximum diameter is 4 cm. Then we used different screwdrivers to carefully make two pairs of holes that were approximately 4 and 6 mm in diameter, respectively. Finally, one big and one small hole on the left side were filled with pork muscle, while the two holes on the right side were filled with pork fat of the same type as that which made up the base.

In the experiment, the transducer rotationally scanned the sample from  $0^\circ$  to  $360^\circ$  with a step size of  $2.25^\circ$ . The detection radius  $r_0$  was 4.3 mm. We used the 160 series of data as shown in Fig. 4(d) to calculate the image by our modified backprojection method.

The reconstructed image is shown in Fig. 5(b). The outline and size of the fat base as well as the sizes and locations of the two muscle pieces are in good agreement with the original sample in Fig. 5(a). Fig. 5(c) shows a line profile for the small piece of muscle in the image. It indicates that the contrast between the fat and the muscle is very high. This high contrast is due to the low microwave absorption capacity of fat and the high absorption capacity of muscle: at 3 GHz, the penetration depth for muscle and fat are 1.2 and 9 cm, respectively. However, the two pieces of fat are not visible in the image [Fig. 5(b)], which means the minute mechanical discontinuity between the boundaries of muscle and fat does not contribute much to the

thermoacoustic signal. On the contrary, discontinuity improves the strength of the echo sounds in pure ultrasound imaging.

### C. Spatial Resolution

Spatial resolution is another important index for biological imaging. We used samples with a set of small thermoacoustic sources to test the resolution. One tested sample is shown in Fig. 6(a), which was also photographed after the experiment was completed.

The sample was made according to the following procedure. First, we cut a thin piece of homogeneous pork fat tissue and made it into an arbitrary shape. Its thickness was 5 mm with a maximum diameter of 4 cm. Then we used a small screwdriver to carefully make a set of small holes about 2 mm in diameter. In the meantime, we prepared a hot solution with 5% gelatin, 0.8% salt, and a drop of dark ink (to improve the photographic properties of the sample). Next, we used an injector to inject a drop of the gelatin solution into each small hole and subsequently blew out the air to make good coupling between the gelatin solution and the fat tissue. After being cooled in room temperature for about 15 min, the gelatin solution was solidified. During the experiment, the transducer also rotationally scanned the sample from  $0^\circ$  to  $360^\circ$  with a step size of  $2.25^\circ$ . The detection radius  $r_0$  was 4.3 mm.

The reconstructed image produced by our modified backprojection method is shown in Fig. 6(b); it also agrees with the original sample well. In particular, the relative locations and sizes of those small thermoacoustic sources are clearly resolved and perfectly match the original ones. Fig. 6(c) shows a reconstructed profile (solid curve) at position  $x = 27.45$  mm of the image Fig. 6(b), which includes two gelatin sources with a distance of about 3 mm. Each gelatin source has a distinct profile in the image. The boundaries between them are clearly imaged. Moreover, the reconstructed profile is in good agreement with the original profile (dashed curve), which was a grayscale profile of the image Fig. 6(b). The half-amplitude line cuts across the reconstructed profile at points  $B_1$ ,  $A_1$ ,  $A_2$ , and  $B_2$ , respectively. The distances  $|A_1B_1| = 1.72$  mm and  $|A_2B_2| = 1.67$  mm in the image are close to the original values of about 1.80 and 1.60 mm, respectively, which were measured in the original objects. Therefore, the width of the profile at the half-amplitude closely measures its physical size.

We here define a resolving criterion to estimate the spatial resolution. The quarter-amplitude line cuts across the profiles at points  $C_1$  and  $C_2$ , respectively, as shown in Fig. 6(c). If the right source moves to the position of the left one, the reconstructed profile is equal to the spatial summation of the profiles of the two sources, because of the linear superposition property of acoustic waves. When point  $C_2$  encounters  $C_1$ , the new amplitude at  $C_2$  or  $C_1$  would reach the half amplitude, and the two sources could still be differentiated. If the right one moves more to the left, the new amplitude between their overlap regions would elevate to more than the half amplitude. When we use a half-amplitude line to cut across the profiles, we get only two points on the far side of each profile, which means that these two sources can no longer be clearly distinguished. Further, when point  $A_1$  touches  $A_2$ , these two sources join as a single object in the image.

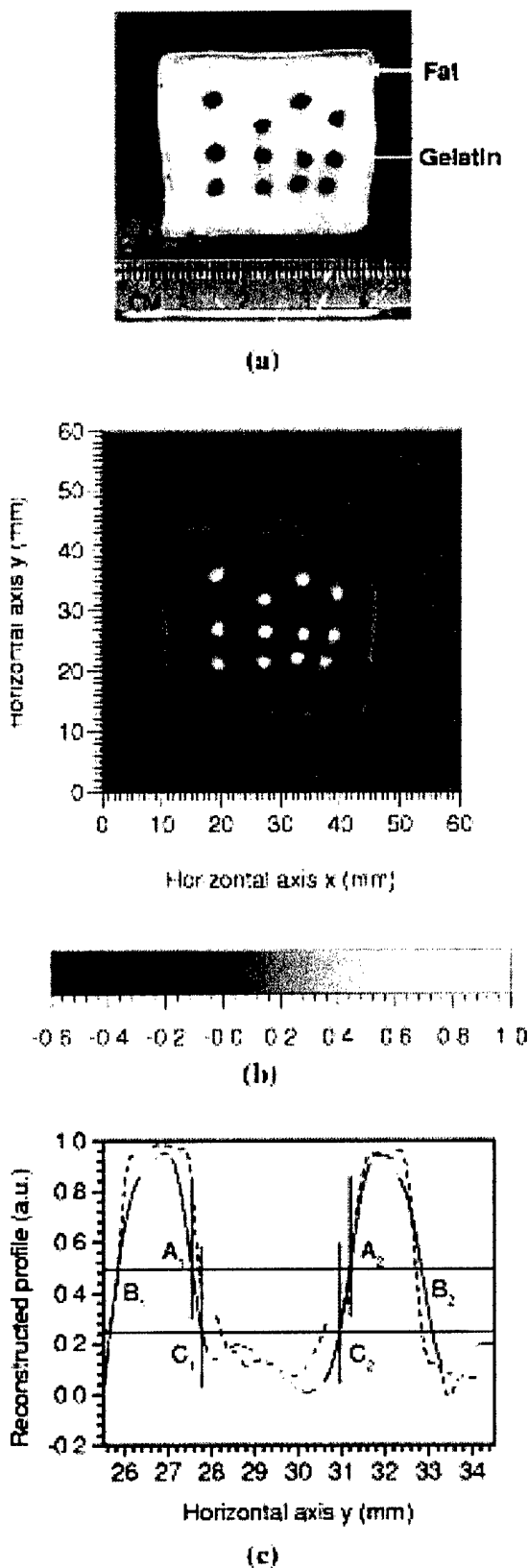
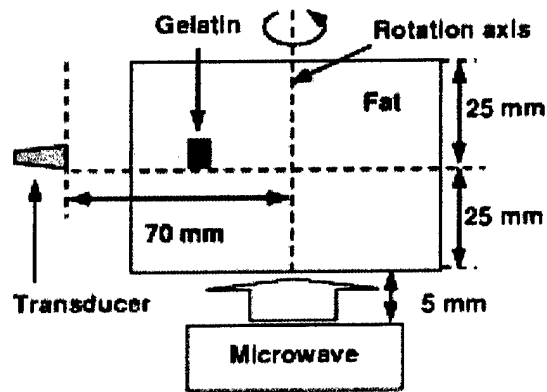
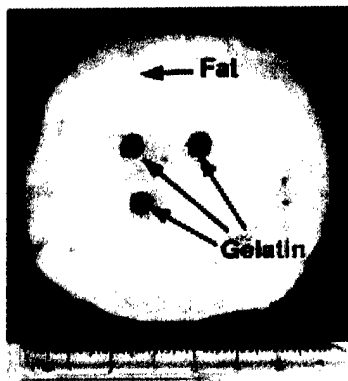


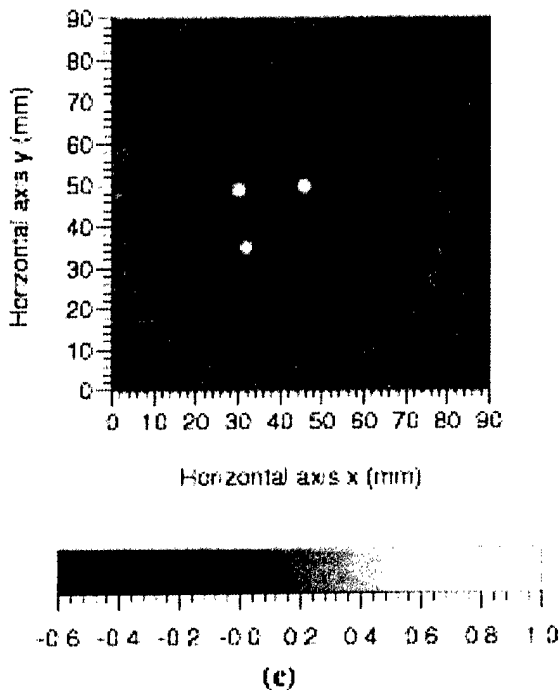
Fig. 6. (a) Cross section of a tissue sample; (b) reconstructed image; and (c) comparison between a line profile (solid curve) of the reconstructed image (b) at  $x = 27.45$  mm and the corresponding grayscale profile (dashed curve) of the original image (a).



(a)



(b)



(c)

Fig. 7. (a) Diagram of the sample structure and the measurement; (b) cross section of the tissue sample; and (c) reconstructed image.

Therefore, the minimum distance that can be differentiated is approximately equal to the summation of the horizontal distance between point  $A_1$  and  $C_1$  and the horizontal distance between

point  $A_2$  and  $C_2$ . We have checked additional pairs of sources resembling those in the image of Fig. 6(b), and found that this minimum distance is less than 0.5 mm. We can, therefore, claim that the spatial resolution in our system reaches less than 0.5 mm, which agrees with the theoretical spatial resolution limit for 1.8-MHz signals whose half wavelength is  $\sim 0.5$  mm with the sound speed of 1.5 mm/ $\mu$ s.

Of course, the detecting transducer has a finite physical size. If it is close to the thermoacoustic sources, it cannot be approximated as a point detector. Its size will blur the images and decrease the spatial resolution. Therefore, in experiments, the transducer must be placed some distance away from the tissue samples. In general, due to the finite size of the transducer, the farther away the transducer is from the detection center, the better the resolution at the expense of the signal strength.

Other limiting factors of spatial resolution include the duration of the microwave pulse and the impulse response of the transducer. In general, using a shorter microwave pulse will produce more high-frequency components in the thermoacoustic signals. The disadvantages resulting from employing a shorter pulse, however, are insufficient energy delivery and a decrease in the signal-to-noise ratio. Selection of the duration of the pulse is dependent on the experimental conditions and measurement systems. In biological tissues, microwaves at 300 MHz $\sim$ 3 GHz with 0.1 $\sim$ 1  $\mu$ s pulse width are often adopted. Therefore, the high-frequency of the thermoacoustic signals reaches several MHz. Such a wide-band transducer for measuring acoustic waves at  $\sim$ MHz is widely available.

#### D. Thick Sample

The advantage of using microwave is its long penetration depth in soft tissue. A microwave can reach a tumor buried inside tissue and heat it to generate thermoacoustic waves. One tested sample is shown in Fig. 7(a). The experiment was conducted according to a procedure similar to the one above. Three small absorbers were buried inside a big fat base. The big pork fat tissue had a maximum diameter of 7 cm. Screwdrivers were used to carefully make three holes about 5 mm in diameter with a depth of 2.5 cm. Next, an injector was used to inject a drop of the same gelatin solution as above into each small hole, and, subsequently, air was blown out to improve the coupling between the gelatin solution and the fat tissue. These gelatin sources were about 5 mm in diameter. After being cooled at room temperature for about 15 min, the gelatin solutions solidified. The photograph of the sample at this stage is shown in Fig. 7(b). Finally, the holes were filled with fat, and the gelatin sources were buried in the fat tissue.

During the experiment, a microwave was transmitted out to the sample from below. The transducer rotationally scanned the sample, including the gelatin sources, from  $0^\circ$  to  $360^\circ$  in a plane as Fig. 7(a) shows. The distance between the transducer and the rotation center was 7 cm. The reconstructed image produced by our modified backprojection method, which agrees well with the original sample, is shown in Fig. 7(c).

The above experiments verified the principle of the modified backprojection algorithm, which implies back projection and coherent summation over spherical surfaces. In particular, a set of circular measurement data would be sufficient to yield a



satisfactory cross-sectional image for a sample with only small absorption sources in the same horizontal plane and a lower absorption background. Of course, for a complicated sample, data from only a circular measurement would be insufficient for 3-D reconstruction unless cylindrical focusing is employed. This limited view problem will be addressed in our future work.

Finally, we must point out that an inhomogeneous acoustic property, such as the speed of sound variation, might result in reconstruction errors. Fortunately, the speed of sound in most soft tissue is relatively constant at  $\sim 1.5$  mm/ $\mu$ s. The above experiments demonstrated that the small speed variations between fat and muscle or gelatin did not result in significant reconstruction artifacts. The reason is that thermoacoustic waves are produced internally by microwave absorption and are propagated one-way to the detectors. Thus, a small speed variation does not affect the travel time of the sound very much in a finite-length path, for example, 10 cm, which is comparable to a typical breast diameter. Therefore, in thermoacoustic tomography, satisfactory contrast and resolution are obtainable even in tissue with a small degree of acoustic inhomogeneity.

## V. CONCLUSION

Pulsed-microwave-induced thermoacoustic tomography of inhomogeneous tissues has been studied. Both an exact inverse solution and a modified backprojection algorithm have been derived, which are based on the data acquired by wide-band point detectors on a spherical surface that encloses the sample under study. A set of experiments on tissue samples has been investigated under a circular measurement configuration. The reconstructed images calculated by the modified backprojection method agree well with the original ones. Results indicate that this technique using reconstruction theory is a powerful imaging method that results in good contrast and good spatial resolution (0.5 mm), which can be used for the investigation of tissues with inhomogeneous microwave absorptions.

## REFERENCES

- [1] L. E. Larsen and J. H. Jacobi, *Medical Applications of Microwave Imaging*. Piscataway, NJ: IEEE Press, 1986.
- [2] K. D. Paulsen and P. M. Meaney, "Nonactive antenna compensation for fixed-array microwave imaging Part I: Model development," *IEEE Trans. Med. Imag.*, vol. 18, pp. 496–507, June 1999.
- [3] P. M. Meaney, K. D. Paulsen, J. T. Chang, M. W. Fanning, and A. Hartov, "Nonactive antenna compensation for fixed-array microwave imaging: Part II Imaging results," *IEEE Trans. Med. Imag.*, vol. 18, pp. 508–518, June 1999.
- [4] F. W. Kremkau, *Diagnostic Ultrasound: Principles and Instruments*. Philadelphia, PA: W. B. Saunders, 1993.
- [5] E. Steen and B. Olstad, "Volume rendering of 3D medical ultrasound data using direct feature mapping," *IEEE Trans. Med. Imag.*, vol. 13, pp. 517–525, June 1994.
- [6] G. Ku and L. V. Wang, "Scanning microwave-induced thermoacoustic tomography: Signal, resolution, and contrast," *Med. Phys.*, vol. 28, pp. 4–10, 2001.
- [7] M. H. Xu, G. Ku, and L. V. Wang, "Microwave-induced thermoacoustic tomography using multi-sector scanning," *Med. Phys.*, vol. 28, pp. 1958–1963, 2001.
- [8] C. G. A. Hoelen and F. F. M. de Mul, "Image reconstruction for photoacoustic scanning of tissue structures," *Appl. Opt.*, vol. 39, no. 31, pp. 5872–5883, Nov. 2000.
- [9] Y. V. Zhulina, "Optimal statistical approach to optoacoustic image reconstruction," *Appl. Opt.*, vol. 39, no. 32, pp. 5971–5977, Nov. 2000.
- [10] R. A. Kruger, D. R. Reinecke, and G. A. Kruger, "Thermoacoustic computed tomography-technical considerations," *Med. Phys.*, vol. 26, no. 9, pp. 1832–1837, 1999.
- [11] S. J. Norton and M. Linzer, "Ultrasonic reflectivity imaging in three dimensions: Exact inverse scattering solutions for plane, cylindrical, and spherical apertures," *IEEE Trans. Biomed. Eng.*, vol. BME-28, pp. 202–220, 1981.
- [12] G. B. Arfken and H. J. Weber, *Mathematical Methods for Physicists*. San Diego, CA: Academic, 1995.
- [13] A. C. Tam, "Application of photoacoustic sensing techniques," *Rev. Mod. Phys.*, vol. 58, pp. 381–431, 1986.
- [14] P. M. Morse and H. Feshbach, *Methods of Theoretical Physics*. New York: McGraw-Hill, 1953.
- [15] Y. Xu, D. Feng, and L. V. Wang, "Exact frequency-domain reconstruction for thermoacoustic tomography: I. Planar geometry," *IEEE Trans. Med. Imag.*, vol. 21, pp. 823–828, July 2002.
- [16] Y. Xu, M. H. Xu, and L. V. Wang, "Exact frequency-domain reconstruction for thermoacoustic tomography: II. Cylindrical geometry," *IEEE Trans. Med. Imag.*, vol. 21, pp. 829–833, July 2002.

# Exact Frequency-Domain Reconstruction for Thermoacoustic Tomography—I: Planar Geometry

Yuan Xu, Dazi Feng, and Lihong V. Wang\*

**Abstract**—We report an exact and fast Fourier-domain reconstruction algorithm for thermoacoustic tomography in a planar configuration assuming thermal confinement and constant acoustic speed. The effects of the finite size of the detector and the finite length of the excitation pulse are explicitly included in the reconstruction algorithm. The algorithm is numerically and experimentally verified. We also demonstrate that the blurring caused by the finite size of the detector surface is the primary limiting factor on the resolution and that it can be compensated for by deconvolution.

**Index Terms**—Fourier-domain reconstruction, planar, thermoacoustic tomography.

## I. INTRODUCTION

USING thermoacoustic tomography (TAT) to image biological tissues has two primary advantages. The first is the high spatial resolution comparable with pure ultrasound imaging. The second advantage results from the large contrast in microwave absorption that exists between cancerous tissue and the normal tissue [1]–[7]. Reviews of TAT and related works [8]–[17] can be found in [11] and [18].

Various reconstruction algorithms for TAT [8], [9], [16], [18], [19] have been reported. Under the approximation that the distance between the detector and the absorbing object is much larger than the dimension of the absorbing object, a three-dimensional (3-D) Radon transform was applied to reconstruct the object in TAT [8]. However, the fact that this approximation may not always hold in real-world situations limits the application of this method. Further, the spatial resolutions of the imaging system using this reconstruction method are limited by blurs [20] caused by the finite size of the transducer surface, the finite width of the stimulating pulse, and the finite bandwidth of the transducers and amplifiers. Among these effects, the blur from the size of the transducer surface is expected to be the largest contributor to the total blur. The analysis of error is

limited in numerical simulations, and, hence, no analytical form was available prior to this work. A time-domain beam-forming technique was applied in one study to image reconstruction for the photoacoustic scanning of tissue structures [9]. A weighted delay-and-sum algorithm was used to account for the near-field effect and to reduce noise. This algorithm is an approximate one, and its lateral resolution is limited by the size of the detector surface. The above reconstructions were implemented in the time domain and consequently are time-consuming, especially in 3-D tomography. TAT was also obtained in a way similar to that used in conventional B-scan ultrasonic imaging, but it had difficulty detecting the boundaries of objects that are oblique to the transducer axis [16]. Exact reconstructions have been implemented for TAT in spherical and cylindrical configurations in the companion papers [18], [19].

Next, we present our studies on an exact and fast reconstruction algorithm using a Fourier transform for TAT in a planar configuration. The reconstruction of an image by Fourier transform has been used in X-ray computed tomography [21], ultrasonic reflectivity imaging [22]–[24], and diffraction tomography [25] successfully. The computation complexity is reduced greatly due to the efficiency of the Fourier transform. We developed image reconstruction by Fourier transform for planar TAT and obtained an exact reconstruction algorithm for the first time. Furthermore, some limitations from experiments, such as the effects of the finite size of the detectors and the finite length of the excitation pulse, are included explicitly in the reconstruction algorithm. The reconstruction algorithm is verified by both numerically simulated and experimental results. Our simulations also demonstrate that the blur due to the finite size of the detector surface, which is a key limiting factor on the resolution of images [9], [20], can be alleviated by deconvolution with respect to the size of the detector surface. Other effects that may cause blurring of images can be treated in a similar way. In our initial experiments, an image in good agreement with the real objects was reconstructed and the deconvolution improved the resolution of the imaging system.

## II. METHODS

### A. Image Reconstruction

Assume that the detector scans within the plane  $z = 0$  and that the object is distributed only in the half space  $z' > 0$ . In order to obtain a spatial resolution of about 1 mm, the microwave pulse should be set to less than  $\sim 1 \mu\text{s}$  because the speed of sound in soft biological tissue is  $\sim 1.5 \text{ mm}/\mu\text{s}$ . For these parameters, the diffusion term in the heat conduction equation is about six orders of magnitude less than the term of the

Manuscript received May 15, 2001; revised May 13, 2002. This work was supported in part by the U.S. Army Medical Research and Material Command under Grant DAMD17-00-1-0455, in part by the National Institutes of Health (NIH) under Grant R01 CA71980 and Grant R21 CA83760, in part by the National Science Foundation (NSF) under Grant BES-9734491, and in part by the Texas Higher Education Coordinating Board under Grant ARP 000512-0123-1999. The Associate Editor responsible for coordinating the review of this paper and recommending its publication was G. Wang. Asterisk indicates corresponding author.

Y. Xu and D. Feng are with the Optical Imaging Laboratory, Department of Biomedical Engineering, Texas A&M University, College Station, TX 77843-3120 USA.

\*L. V. Wang is with the Optical Imaging Laboratory, Department of Biomedical Engineering, Texas A&M University, 3120 TAMU, College Station, TX 77843-3120 USA (e-mail: LWang@tamu.edu).

Publisher Item Identifier 10.1109/TMI.2002.801172.

first-derivative of the temperature [26]. Therefore, heat conduction can be ignored. This is known as the assumption of thermal confinement. In this case, the acoustic wave  $p(\mathbf{r}, \bar{t})$  is related to microwave absorption  $H(\mathbf{r}, \bar{t})$  by the following wave equation [26]:

$$\frac{\partial^2 p(\mathbf{r}, \bar{t})}{\partial \bar{t}^2} - \nabla^2 p(\mathbf{r}, \bar{t}) = \frac{\beta v_s}{C} \frac{\partial H(\mathbf{r}, \bar{t})}{\partial \bar{t}} \quad (1)$$

where  $\bar{t} = tv_s$ ,  $v_s$  is the acoustic speed,  $C$  is the specific heat, and  $\beta$  is the coefficient of volume thermal expansion. In (1), the acoustic speed is assumed constant, which will be further addressed in the discussion section. Equation (1) can be rewritten in terms of  $H(\mathbf{r}', \bar{t})$ :

$$p(\mathbf{r}, \bar{t}) = \frac{\beta v_s}{4\pi C} \iiint \frac{\partial H(\mathbf{r}', t')}{\partial t'} \frac{d\mathbf{r}'}{|\mathbf{r} - \mathbf{r}'|} \quad (2)$$

where  $t' = \bar{t} - |\mathbf{r} - \mathbf{r}'|/v_s$ . The source term  $H(\mathbf{r}', \bar{t})$  can further be written as the product of a purely spatial and a purely temporal component, i.e.,

$$H(\mathbf{r}', \bar{t}) = I_0 \varphi(\mathbf{r}') \eta(\bar{t}) \quad (3)$$

where  $I_0$  is a scaling factor proportional to the incident radiation intensity,  $\varphi(\mathbf{r}')$  describes the microwave absorption properties of the medium at  $\mathbf{r}'$ .  $\eta(\bar{t})$  describes the shape of the irradiating pulse and is a nonnegative function whose integration over time equals the pulse energy. Substituting (3) into (2) results in

$$p(\mathbf{r}, \bar{t}) = \frac{I_0 \beta v_s}{4\pi C} \iiint \varphi(\mathbf{r}') \frac{d\eta(t')}{dt'} \frac{d\mathbf{r}'}{|\mathbf{r} - \mathbf{r}'|}. \quad (4)$$

We proceed by transforming the time-dependent wave equation into the temporal-frequency domain. Denoting the Fourier transforms of  $p$  and  $\eta$  by  $\bar{p}$  and  $\bar{\eta}$ , we have

$$p(\mathbf{r}, \bar{t}) = \int_{-\infty}^{\infty} \bar{p}(\mathbf{r}, k) \exp(ik\bar{t}) dk \quad (5)$$

$$\eta(\bar{t}) = \int_{-\infty}^{\infty} \bar{\eta}(k) \exp(ik\bar{t}) dk. \quad (6)$$

Substituting (5) and (6) into (4) results in

$$\bar{p}(\mathbf{r}, k) = \frac{i\beta v_s I_0 k \bar{\eta}(k)}{4\pi C} \iiint \varphi(\mathbf{r}') \frac{\exp(-ik|\mathbf{r} - \mathbf{r}'|)}{|\mathbf{r} - \mathbf{r}'|} d\mathbf{r}'. \quad (7)$$

If the acoustic signals are collected along a line or in a plane, for example at  $z = 0$ , following the line of Norton and Linzer in [22], it can be shown that for the case  $|k| > \rho$  and  $z' > 0$

$$\bar{P}(u, v, k) = \frac{\beta v_s I_0 k \bar{\eta}(k) \text{sgn}(k)}{2C \sqrt{k^2 - \rho^2}} \cdot \int_0^{\infty} \Phi(u, v, z') \exp(-iz' \text{sgn}(k) \sqrt{k^2 - \rho^2}) dz' \quad (8)$$

where  $\rho^2 = u^2 + v^2$ ,  $\text{sgn}(k)$  is the signum function

$$\bar{P}(u, v, k) = \frac{1}{(2\pi)^2} \iint \bar{p}(x, y, 0, k) \cdot \exp(-i(ux + vy)) dx dy \quad (9)$$

and

$$\Phi(u, v, z') = \frac{1}{(2\pi)^2} \iint \varphi(\mathbf{r}') \cdot \exp(-i(ux' + vy')) dx' dy'. \quad (10)$$

Equation (8) can further be simplified to

$$\bar{P}(u, v, k) = \frac{\pi \beta v_s I_0 k \bar{\eta}(k) \text{sgn}(k) \Phi_1(u, v, \text{sgn}(k) \sqrt{k^2 - \rho^2})}{C \sqrt{k^2 - \rho^2}} \quad (11)$$

where

$$\Phi_1(u, v, w) = \frac{1}{2\pi} \int_{-\infty}^{\infty} \Phi(u, v, z') \exp(-iws') dz'. \quad (12)$$

The lower limit of the above integration is changed from 0 to  $-\infty$  because  $\Phi(u, v, z') = 0$  when  $z' < 0$ . Equation (11) gives an exact mapping relation between the spectrum of the collected signals and the spectrum of the distribution of microwave energy deposition and is the essence of our reconstruction method. However, (11) stands only if the acoustic detector is a point detector. In practice, the detector is of finite size, whose surface shape can be described by  $R(x, y)$ . The signal from the detector  $p_d(x, y, t)$  can be expressed as an integral of the acoustic wave  $p(\mathbf{r}, t)$  over the detector surface

$$p_d(x, y, t) = \iint_s p(x', y', t) R(x' - x, y' - y) dx' dy'. \quad (13)$$

After transforming (13) into the temporal- and spatial-frequency domain, we have

$$\bar{P}_d(u, v, k) = 4\pi^2 \bar{P}(u, v, k) \bar{R}(-u, -v) \quad (14)$$

where  $\bar{P}_d(u, v, k)$  is the temporal and spatial Fourier transform of  $p_d(x, y, t)$ , and  $\bar{R}(u, v)$  is the spatial Fourier transform of  $R(x, y)$ . Substituting (14) into (11) results in

$$\bar{P}_d(u, v, k) = \frac{4\pi^3 \beta v_s I_0 k \bar{\eta}(k) \text{sgn}(k) \bar{R}(-u, -v) \Phi_1(u, v, \text{sgn}(k) \sqrt{k^2 - \rho^2})}{C \sqrt{k^2 - \rho^2}}. \quad (15)$$

Mapping the  $(u, v, k)$  space into the  $(u, v, w)$  space by the relation

$$w = \text{sgn}(k) \sqrt{k^2 - \rho^2} \quad (16)$$

yields an explicit expression for  $\Phi_1$

$$\Phi_1(u, v, w) = \frac{C w \bar{P}_d(u, v, \text{sgn}(w) \sqrt{w^2 + \rho^2})}{4\pi^3 \beta v_s I_0 \text{sgn}(w) \sqrt{w^2 + \rho^2} \bar{\eta}(\text{sgn}(w) \sqrt{w^2 + \rho^2}) \bar{R}(-u, -v)}. \quad (17)$$

At last, the distribution of the microwave energy deposition can be reconstructed from  $\Phi_1$  by 3-D inverse Fourier transform. Equation (17) gives an exact reconstruction algorithm for planar

TAT for the first time. Furthermore, the effects of the finite size of the detectors and the finite length of the excitation pulse are included explicitly. From (17), it can be inferred that the reconstructed image spectrum  $\Phi_d(u, v, w)$  from the experimental data without the consideration of these two effects, as was presented by previous researchers [9], [20], is related to the actual image spectrum  $\Phi_1(u, v, w)$  by

$$\Phi_d(u, v, w) = 4\pi^2 \bar{\eta} \left( \text{sgn}(w) \sqrt{w^2 + \rho^2} \right) \bar{R}(-u, -v) \Phi_1(u, v, w). \quad (18)$$

Both of the effects result in multiplications of a function to the actual image spectrum in the frequency domain. They are equivalent to convolutions in the spatial domain, which blur the reconstructed image. However, given the pulse shape and the surface configuration of the detector surface, the two effects can be reduced by deconvolution.

To summarize, the reconstruction procedure consists of the following steps.

- 1) The signal from the detector  $p_d(x, y, \bar{t})$  is Fourier transformed with respect to  $\bar{t}$  to yield  $\bar{p}_d(x, y, k)$ . Deconvolution with respect to the finite pulse length can be implemented immediately after the Fourier transform.
- 2)  $\bar{p}_d(x, y, k)$  is Fourier transformed with respect to  $x$  and  $y$ , yielding  $\bar{P}_d(u, v, k)$ .
- 3) According to (16) and (17),  $\bar{P}_d(u, v, k)$  is mapped to  $\Phi_d(u, v, w)$ .
- 4)  $\Phi_d(u, v, w)$  is deconvoluted with respect to the finite size of the detector, giving  $\Phi_1(u, v, w)$ .
- 5)  $\Phi_1(u, v, w)$  is inversely Fourier transformed with respect to  $u, v, w$  to yield  $\varphi(x', y', z')$ .

The order of steps 4) and 5) can be exchanged so that more stable deconvolution algorithms can be applied. In numerical calculations,  $\bar{P}_d(u, v, k)$  is obtained only at discrete points; hence the mapping from  $\bar{P}_d(u, v, k)$  to  $\Phi_d(u, v, w)$  needs interpolation, which can be a major source of distortion.

### B. System Setting

The experimental setup was reported in [27] and, for convenience, is only briefly described here (Fig. 1). The  $x$  axis points perpendicularly to the drawing plane; the  $y$  axis points to the right in the plane; and the  $z$  axis points downward along the acoustic axis. Microwave pulses are transmitted by a 9-GHz microwave generator. The pulse width is 0.5  $\mu$ s. The object to be imaged is a cylinder of pork fat containing a thin layer of connective tissue and six yellow microstructures. The diameter of the cylinder fat is 14 mm and the length in the  $x$  direction 30 mm. The cylinder was immersed in mineral oil in a plexiglass tank. The central frequency of the ultrasonic transducer (Panametrics) is 2.25 MHz; the bandwidth 1.8 MHz; and the diameter of the active element 6 mm. More details about the system can be found in [27].

## III. RESULTS AND DISCUSSION

Our method was applied to reconstructing images from both the simulated and the experimental data in a two-dimensional (2-D) case, where the imaged objects were uniform along the  $x$

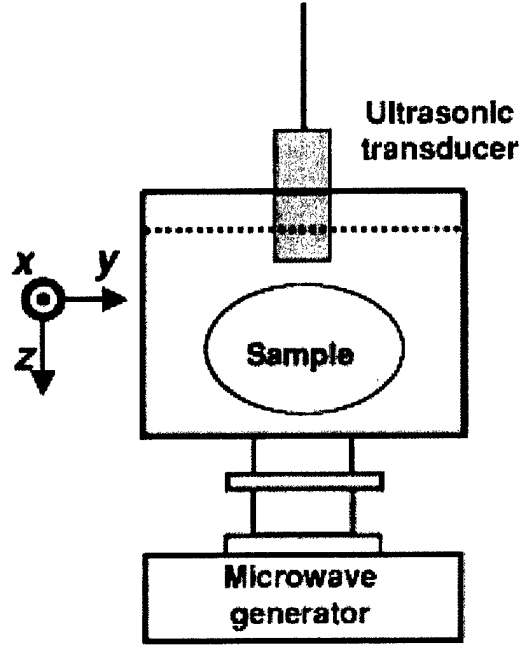


Fig. 1. Experimental setup for TAT.

axis. Because the blur due to the finite size of the detector surface is a limiting factor on the resolution of images, we demonstrated how deconvolution with respect to the detector surface can deblur the images. We chose the 2-D case here because both the computational and experimental complexity can be reduced more in the 2-D case than in the 3-D one. Nevertheless, the extension of the conclusions of the 2-D case to the 3-D one is straightforward.

### A. Simulation

The thermoacoustic imaging of two cylinders was numerically simulated. Cylinders were chosen because the analytical expression for their thermoacoustic signal is available [28]. In the simulations, the temporal-frequency range was from near 0 to 1.5 MHz, which was in accordance with the experimental one and with our previous experiments [11]. Two simulations were run. The first one was to test our reconstruction algorithm under an ideal experimental condition, which is noiseless and does not consider any experimental limitations on the detectors. In the second case, the effect of the finite size of the detectors on the imaging was studied while noise was also added. Deconvolution with respect to the finite size of the detector surface was applied to improve the lateral resolution of the blurred image. Since energy deposition is a positive value, only the positive components of the reconstructed image were retained, and the others were set to zero.

In step 3) of the reconstruction, which is the mapping from  $\bar{P}_d(u, v, k)$  to  $\Phi_d(u, v, w)$ , linear interpolation was applied. By adopting the zero-padding technique [25] for the time-domain data, one can increase the sampling density in the  $k$ -space and, consequently, obtain a better performance of the interpolation in the  $k$ -space. In the reconstruction from the simulation data and experimental data, we appended to the end of the data the same number of zeros as in the original collected data, so that

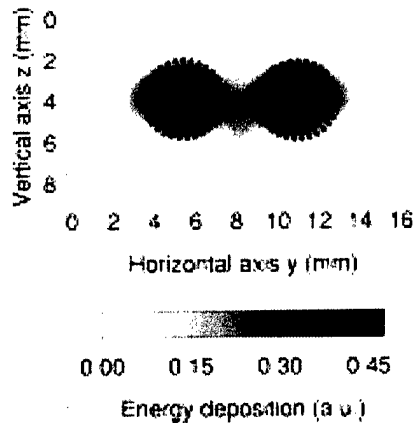


Fig. 2. The reconstructed image of the cross-section of two cylinders with a radius of 2 mm and the centers separated by 5.5 mm under ideal experimental conditions.

the sampling density in the  $k$ -space was doubled. By utilizing the Wiener filtering method [29], deconvolution with respect to the finite pulse length was implemented immediately after the Fourier transform with respect to time in step 1). As the deconvolution with respect to the finite size of the detector surface is much more unstable than the deconvolution with respect to the finite pulse length, we have tried two methods of deconvolution: the Wiener filtering method and the piecewise polynomial truncated singular value decomposition (PP-TSVD) [30] method. The first method can be implemented in the spatial-frequency domain and is more computationally efficient than the second, but the performance of the second method is much better, as it can restore sharp boundaries blurred by the convolution while avoiding the appearance of artificial oscillations in an unstable deconvolution. Therefore, we adopted the PP-TSVD method to process the images. Since the models in our simulation and experiment were uniform along the  $x$  axis, one-dimension deconvolution was applied.

Fig. 2 shows the reconstructed image from the simulated data under the ideal experimental condition, where the radius of the two cylinders was 2 mm; the distance between the centers of the cylinders was 5.5 mm; the centers of the cylinders were positioned in the plane of  $z = 10$  mm; the scanning range of the detector along the  $y$  axis was 90 mm with a step size of 0.5 mm; and the thermoacoustic signals were sampled for 40  $\mu$ s at a sampling rate of 50 MHz. The reconstructed image is in good agreement with the real objects, whose outlines are plotted as dotted circles in Fig. 2. The dimension of the cylinders is 3.75 mm along the  $z$  direction and 4.7 mm along the  $y$  direction. The cylinder is a little deformed laterally, which is due to the finite scanning range of the detector.

Fig. 3 shows the images before and after deconvolution with respect to the finite size of the detector surface in a case similar to our experimental conditions. The noise was added to the thermoacoustic signals, and the signal-to-noise ratio (SNR) was 50; the diameter of the detector was 6 mm. All of the other parameters were the same as those in the first case. The image before deconvolution is shown in Fig. 3(a). The dimension of the images of the objects is 3.5 mm along the  $y$  axis, which agrees well with the real one, 4 mm. However, along the  $z$  axis, the images

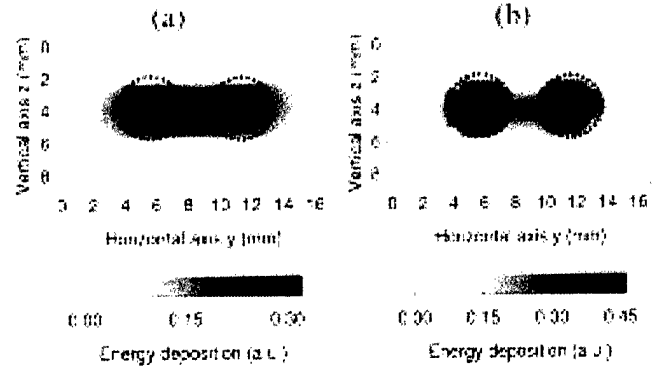


Fig. 3. The reconstructed images for the same two cylinders as in Fig. 2 from noisy data (a) before and (b) after the deconvolution with respect to the detector surface.

of the two cylinders were blurred and consequently merged into one, which is predicted by our analysis of the effect of the finite size of the detector. The image shows no clear boundaries of the objects along the  $y$  axis. After deconvolution, the lateral boundaries of the objects become very clear and the width of the objects in Fig. 3(b) is 4.1 mm, which is quite close to reality. Furthermore, the two objects can be distinguished clearly. After comparing Fig. 3(a) with (b), it seems that the ghost images become slightly more obvious, which is a disadvantage of deconvolution. Nevertheless, it is obvious that deconvolution with respect to the finite size of the detector surface can improve the lateral resolution greatly.

In Figs. 2 and 3, there are some ghost images. In principle, our reconstruction method is exact under the assumption of thermal confinement and constant acoustic speed. However, several factors may introduce distortions. First, as mentioned at the end of part Section II-A, the mapping from  $\bar{P}_d(u, v, k)$  to  $\Phi_d(u, v, w)$  needs interpolation, which is a major source of distortion. This distortion can be reduced by increasing sampling time or applying a better interpolation algorithm in the mapping. Second, in experiments, the detector cannot be scanned over the whole plane. Nevertheless, Fig. 2 shows that collecting data within a finite area of the collection plane can produce images of sufficient definition to determine the configuration and position of the objects.

## B. Experimental Result

Fig. 4 shows the experimental result. The images before and after deconvolution with respect to the finite size of the detector surface are shown in Fig. 4(a) and (b), respectively. Fig. 4(c) is the cross section of the biological tissue, which was a cylinder with a radius of about 14 mm and 3 cm long. It consisted of two parts of fat separated by a very thin layer of connective tissue, which is labeled as (7) in the middle of the sample. There were some yellow microstructures among the fat, labeled from (1)–(6), respectively. Fig. 4(a) is the image reconstructed from the experimental data before deconvolution. The connective tissue between the two parts of fat and the yellow microstructures are imaged clearly. The dimension of the image is 16.4 mm along the  $z$  direction and 19.2 mm along the  $y$  direction. However, it is obvious that the image before deconvolution is blurred along the  $y$  axis, which makes

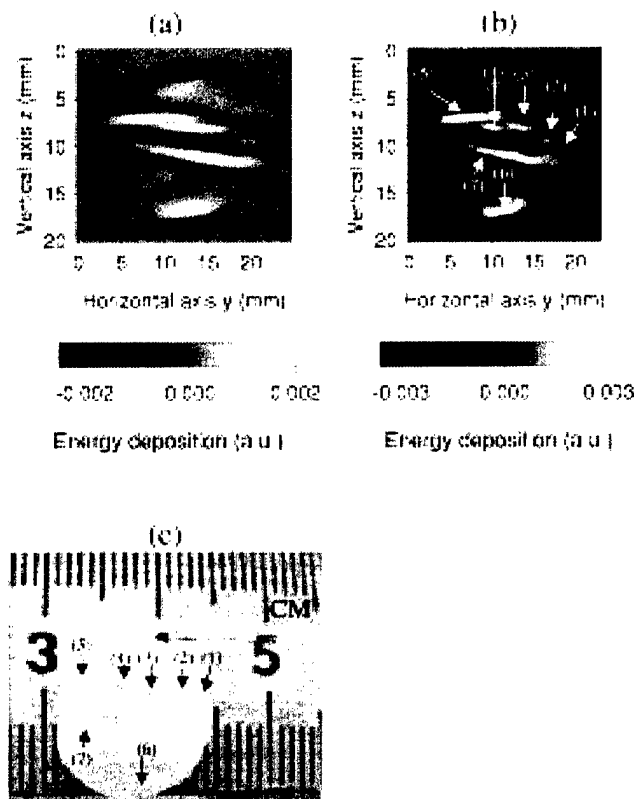


Fig. 4. The reconstructed images from the experimental data (a) before and (b) after the deconvolution with respect to the detector surface; (c) the cross section of a cylinder of fat sample containing six yellow microstructures labeled from (1)–(6) and a layer of connective tissue in the middle labeled as (7).

the lateral boundaries unclear and the yellow microstructures (1) and (2), (3) and (4) merge into one object, respectively. The lateral resolution of the image needs to be improved. Consequently, deconvolution with respect to the finite size of the detector surface was applied to Fig. 4(a), and the result is shown in Fig. 4(b). The lateral resolution of the image after deconvolution is much improved. The merged objects can be distinguished clearly, and the lateral boundaries of the cylinder become much clearer. The dimension of the image is 16.4 mm along the  $z$  direction and 16.7 mm along the  $y$  direction.

### C. Discussion

There are several advantages of our reconstruction method. The first one is that it is an exact reconstruction algorithm. Unlike other reconstruction methods for TAT that are approximate ones, our reconstruction method provides a solid base for analyzing and improving the quality of reconstructed images. Furthermore, the exact reconstruction method has a broader application than the approximate ones. For example, in both our simulation and experiment, the closest distance between the objects and the detectors was only about 1 cm; this is possible because in principle there is no limitation on the detector–object distance in our method. In other words, the detector can be placed very close to the object to ensure a better SNR. The second advantage of our method is that it can explicitly include the effect of many limitations from the experiment, such as the finite size of detector surface, the microwave pulse

length, and the finite frequency response range of the detector. Actually, these analyses are also valid for other approximate reconstruction methods as long as the other reconstruction methods are able to produce images approximating the real objects. Consequently, our analysis of the blur caused by the various experimental limitations can also be very useful for eliminating the limitations in other reconstruction methods. Lastly, since the reconstruction in our method is implemented in the frequency domain, the efficiency of computation is much better than the algorithm implemented in the time domain due to the use of the efficient Fourier transformation in our method. This is especially important for real-time 3-D imaging.

From the above images, it can be seen that there is no speckle in the reconstructed image. Speckles are an important factor limiting the quality of pure ultrasonic imaging. In our technology, the detected signals are directly from the primary acoustic waves rather than reflective or scattered waves. Further, the temporal frequency of the acoustic signals lies in a range from 0 to 1.5 MHz, which is only weakly scattered in the tissues. The above two factors guarantee that there is no obvious speckle in our experimental images. However, the issue of image speckle in more realistic medical imaging applications of our algorithm is a topic for future consideration.

The formulas in this paper are for TAT in planar geometry only. However, for cylindrical geometry [19], we can predict that the lateral resolution of images can also be improved by deconvolution with respect to the detector surface, where the deconvolution is carried out in a cylindrical surface instead of a plane. For spherical geometry [18], similar work can be conducted as well.

For many medical imaging applications, the acoustic speed may not be constant. For example, the acoustic speed inside the female breast may typically exhibit a 10% variation; however, our simulation, to be reported elsewhere, showed that the image distortion is relatively small.

### IV. CONCLUSION

We developed a Fourier-domain reconstruction for TAT and obtained an exact and fast reconstruction algorithm. The effects of the finite size of the detectors and the finite length of the excitation pulse were included explicitly in the reconstruction algorithm. The reconstruction algorithm was verified by both numerical simulations and experimental results. Our simulations demonstrated that the blurring caused by the finite size of the detector surface, which is a key limiting factor on the resolution of images, can be alleviated by deconvolution with respect to the detector surface. Other effects that may cause the blur of the images can be treated in a similar way. In the initial experiment, an image in good agreement with the real objects was reconstructed and the deconvolution improved the resolution of the imaging system. The method can also be extended to other configurations of data collection.

### REFERENCES

- [1] W. Joines, R. Jirtle, M. Rafal, and D. Schaeffer, "Microwave power absorption differences between normal and malignant tissue," *Radiation Oncol. Biol. Phys.*, vol. 6, pp. 681–687, 1980.

- [2] S. Chaudhary, R. Mishra, A. Swarup, and J. Thomas, "Dielectric properties of normal human breast tissues at radiowave and microwave frequencies," *Indian J. Biochem. Biophys.*, vol. 21, pp. 76–79, 1984.
- [3] W. Joines, Y. Zhang, C. Li, and R. Jirtle, "The measured electrical properties of normal and malignant human tissues from 50–900 MHz," *Med. Phys.*, vol. 21, pp. 547–550, 1994.
- [4] L. E. Larsen and J. H. Jacobi, Eds., *Medical Applications of Microwave Imaging*. Piscataway, NJ: IEEE Press, 1986.
- [5] S. Caorsi, A. Frattoni, G. L. Gagnani, E. Nortino, and M. Pastorino, "Numerical algorithm for dielectric-permittivity microwave imaging of inhomogeneous biological bodies," *Med. Biol. Eng. Comput.*, vol. NS-29, pp. 37–44, 1991.
- [6] M. S. Hawley, A. Broquetas, L. Jofre, J. C. Bolomey, and G. Gaboriaud, "Microwave imaging of tissue blood content changes," *J. Biomed. Eng.*, vol. 13, pp. 197–202, 1991.
- [7] P. M. Meaney, K. D. Paulsen, and J. T. Chang, "Near-field microwave imaging of biologically-based materials using a monopole transceiver system," *IEEE Trans. Microwave Theory Tech.*, vol. 46, pp. 31–45, Jan 1998.
- [8] R. A. Kruger, P. Liu, Y. R. Fang, and C. R. Appledorn, "Photoacoustic ultrasound (PAUS)—Reconstruction tomography," *Med. Phys.*, vol. 22, pp. 1605–1609, 1995.
- [9] C. G. A. Hoelen, F. F. M. Demul, R. Pongers, and A. Dekker, "Three-dimensional photoacoustic imaging of blood vessels in tissue," *Opt. Lett.*, vol. 23, pp. 648–650, 1998.
- [10] A. A. Karabutov, E. V. Savateeva, N. B. Podymova, and A. A. Oraevsky, "Backward mode detection of laser-induced wide-band ultrasonic transients with optoacoustic transducer," *J. Appl. Phys.*, vol. 87, pp. 2003–2014, 2000.
- [11] Y. Xu and L.-H. V. Wang, "Signal processing in scanning thermoacoustic tomography in biological tissues," *Med. Phys.*, vol. 28, pp. 1519–1524, 2001.
- [12] T. Bowen, L. Nasoni, A. E. Pifer, and G. H. Sembrock, "Some experimental results on the thermoacoustic imaging of soft tissue-equivalent phantoms," in *Proc. IEEE Ultrasonics Symp.*, vol. 2, 1981, pp. 823–827.
- [13] J. C. Lin and K. H. Chan, "Microwave thermoelastic tissue imaging—System design," *IEEE Trans. Microwave Theory Tech.*, vol. MTT-32, pp. 854–860, 1984.
- [14] R. A. Kruger, D. R. Reinecke, and G. A. Kruger, "Thermoacoustic computed tomography: Technical considerations," *Med. Phys.*, vol. 26, pp. 1832–1837, 1999.
- [15] L.-H. V. Wang, X. Zhao, H. Sun, and G. Ku, "Microwave-induced acoustic imaging of biological tissues," *Rev. Sci. Instrum.*, vol. 70, pp. 3744–3748, 1999.
- [16] G. Ku and L.-H. V. Wang, "Scanning thermoacoustic tomography in biological tissue," *Med. Phys.*, vol. 27, pp. 1195–1202, 2000.
- [17] —, "Scanning microwave-induced thermoacoustic tomography: Signal, resolution, and contrast," *Med. Phys.*, vol. 28, pp. 4–10, 2001.
- [18] M. Xu and L.-H. V. Wang, "Time-domain reconstruction for thermoacoustic tomography in a spherical geometry," *IEEE Trans. Med. Imag.*, vol. 21, pp. 814–822, July 2002.
- [19] Y. Xu, M. Xu, and L.-H. V. Wang, "Exact frequency-domain reconstruction for thermoacoustic tomography—II: Cylindrical geometry," *IEEE Trans. Med. Imag.*, vol. 21, pp. 829–833, July 2002.
- [20] W. J. Kiser, Jr. and R. A. Kruger, "Thermoacoustic computed tomography—limits to spatial resolution," *SPIE*, vol. 3659, pp. 895–905, 1999.
- [21] H. Stark, J. W. Woods, I. Paul, and R. Hingorani, "Direct Fourier reconstruction in computer tomography," *IEEE Trans. Acoust. Speech Signal Processing*, vol. ASSP-29, pp. 237–245, 1981.
- [22] S. J. Norton and M. Linzer, "Ultrasonic reflectivity imaging in three dimensions: Exact inverse scattering solution for plane, cylindrical and spherical aperture," *IEEE Trans. Biomed. Eng.*, vol. BME-28, pp. 202–220, Feb. 1981.
- [23] K. Nagai, "A new synthetic-aperture focusing method for ultrasonic b-scan imaging by the Fourier transform," *IEEE Trans. Sonics Ultrason.*, vol. SU-32, pp. 531–536, 1985.
- [24] J. Lu, "Experimental study of high frame rate imaging with limited diffraction beams," *IEEE Trans. Ultrason. Ferroel. Frequency Control*, vol. 45, pp. 84–97, Jan. 1998.
- [25] S. X. Pan and A. C. Kak, "A computational study of reconstruction algorithms for diffraction tomography: Interpolation versus filtered backprojection," *IEEE Trans. Acoust. Speech Signal Processing*, vol. ASSP-31, pp. 1262–1275, 1983.
- [26] V. E. Gusev and A. A. Karabutov, *Laser Optoacoustics*. New York: Amer. Inst. Phys., 1993.
- [27] D. Feng, Y. Xu, G. Ku, and L.-H. V. Wang, "Microwave-induced thermoacoustic tomography: Reconstruction by synthetic aperture," *Med. Phys.*, vol. 28, pp. 2427–2431, 2001.
- [28] G. J. Diebold, M. I. Khan, and S. M. Park, "Photoacoustic signatures of particulate matter: Optical production of acoustic monopole radiation," *Science*, vol. 250, pp. 101–104, 1990.
- [29] A. K. Jain, *Fundamentals of Digital Image Processing*. Englewood Cliffs, NJ: Prentice Hall, 1989.
- [30] P. C. Hansen and K. Mosegaard, "Piecewise polynomial solutions without *priori* breakpoints," *Num. Lin. Alg. Applicat.*, vol. 3, pp. 513–524, 1996.

# Exact Frequency-Domain Reconstruction for Thermoacoustic Tomography—II: Cylindrical Geometry

Yuan Xu, Minghua Xu, and Lihong V. Wang\*

**Abstract**—Microwave-induced thermoacoustic tomography (TAT) in a cylindrical configuration is developed to image biological tissue. Thermoacoustic signals are acquired by scanning a flat ultrasonic transducer. Using a new expansion of a spherical wave in cylindrical coordinates, we apply the Fourier and Hankel transforms to TAT and obtain an exact frequency-domain reconstruction method. The effect of discrete spatial sampling on image quality is analyzed. An aliasing-proof reconstruction method is proposed. Numerical and experimental results are included.

**Index Terms**—Cylindrical, frequency-domain reconstruction, thermoacoustic tomography.

## I. INTRODUCTION

**T**HERMOACOUSTIC tomography (TAT) combines the strength of traditional microwave imaging and ultrasound imaging [1]–[14]. Reviews on TAT and related techniques can be found in [11], [12], [14]. Recently, we derived exact reconstruction algorithms for TAT in both planar and spherical configurations; these are reported in the companion papers [11], [12]. We recognize, however, that in some applications such as the imaging of the limbs, a cylindrical scanning surface may be more appropriate. In this paper, using a new expansion formula in cylindrical coordinates, we derive a frequency-domain reconstruction algorithm [15]–[19] and report our numerical and experimental results in two-dimensional (2-D) cases.

## II. METHODS

We assume that the detector scans on a cylindrical surface with a radius of  $\rho$ , which encircles all microwave absorbing objects. In our paper, a coordinate with a prime refers to the position in an imaged object, while a coordinate without a prime refers to that of a detector. In the case of thermal confinement,

the temporal spectrum of acoustic field  $\bar{p}(\mathbf{r}, k)$  is related to the microwave absorption distribution  $\varphi(\mathbf{r}')$  by the following equation [11]:

$$\bar{p}(\mathbf{r}, k) = \frac{i\beta v_s I_0 k \bar{\eta}(k)}{4\pi C} \iiint \varphi(\mathbf{r}') \frac{\exp(-ik|\mathbf{r} - \mathbf{r}'|)}{|\mathbf{r} - \mathbf{r}'|} d\mathbf{r}' \quad (1)$$

where the symbols are defined as in [11]. Cylindrical coordinates are used in the following derivation, where  $z$  is shown in [12, Fig. 2], and  $\rho, \phi$  are the polar coordinates within the  $x$ - $y$  plane. Following the derivation of the series expansion of  $1/|\mathbf{r} - \mathbf{r}'|$  [20], we obtained the following new identity for a series expansion of a spherical wave in a cylindrical coordinate system (see the Appendix for the derivation):

$$\begin{aligned} & \frac{\exp(-ik|\mathbf{r} - \mathbf{r}'|)}{4\pi|\mathbf{r} - \mathbf{r}'|} \\ &= \frac{-i}{8\pi} \int_{-\infty}^{\infty} dk_z \exp[-ik_z(z' - z)] \\ & \cdot \sum_{m=-\infty}^{\infty} A(m, \mu\rho', \mu\rho) \exp[-im(\phi' - \phi)] \end{aligned} \quad (2)$$

where  $\mu = \text{sgn}(k)\sqrt{|k|^2 - k_z^2}$ ;  $\text{sgn}()$  is the signum function; and  $A$  is the function defined as

$$A(m, \mu\rho', \mu\rho) = \begin{cases} J_m(\mu\rho')H_m^2(\mu\rho), & \text{if } |k| \geq |k_z| \\ \frac{2i}{\pi} I_m(|\mu|\rho')K_m(|\mu|\rho), & \text{if } |k| < |k_z| \end{cases}$$

where  $J_m, H_m^2, I_m$ , and  $K_m$  are the  $m$ th-order Bessel, second-kind, and modified Bessel functions, respectively. It has been assumed in the above two equations that  $\rho > \rho'$ . Substituting (2) into (1) results in

$$\begin{aligned} \bar{p}(\mathbf{r}, k) &= \frac{\beta v_s I_0 k \bar{\eta}(k) \text{sgn}(k)}{8\pi C} \iiint d\mathbf{r}' \varphi(\mathbf{r}') \\ & \cdot \int_{-\infty}^{\infty} dk_z \exp[-ik_z(z' - z)] \\ & \cdot \sum_{m=-\infty}^{\infty} A(m, \mu\rho', \mu\rho) \exp[-im(\phi' - \phi)]. \end{aligned} \quad (3)$$

The  $|k| \geq |k_z|$  part of the integration with respect to  $k_z$  represents the contribution from the propagation wave, while the  $|k| < |k_z|$  part represents the evanescent wave. As the evanescent wave decays rapidly at a distance several wavelengths from

Manuscript received July 30, 2001; revised May 13, 2002. This work was supported in part by the U.S. Army Medical Research and Materiel Command under Grant DAMD17-00-1-0455, in part by the National Institutes of Health (NIH) under Grant R01 CA71980 and Grant R21 CA83760, in part by the National Science Foundation (NSF) under Grant BES-9734491, and in part by the Texas Higher Education Coordinating Board under Grant ARP 000512-0123-1999. The Associate Editor responsible for coordinating the review of this paper and recommending its publication was G. Wang. Asterisk indicates corresponding author.

Y. Xu and M. Xu are with the Optical Imaging Laboratory, Department of Biomedical Engineering, Texas A&M University, College Station, TX 77843-3120 USA.

\*L. Wang is with the Optical Imaging Laboratory, Department of Biomedical Engineering, Texas A&M University, 3120 TAMU, College Station, TX 77843-3120 USA (e-mail: LWang@tamu.edu).

Publisher Item Identifier 10.1109/TMI.2002.801171.



the source, it is not suitable for thermoacoustic imaging. For the case of  $|k| \geq |k_z|$ , after Fourier transforming both sides of the above equation with respect to  $\phi$  and  $z$ , we have

$$\bar{p}_1(m, k_z, k) = \frac{\beta v_s I_0 k \bar{\eta}(k) H_m^2(\mu\rho)}{8\pi C} \cdot \int_0^\infty d\rho' \rho' \varphi_1(m, k_z, \rho') J_m(\mu\rho') \quad (4)$$

where  $\bar{p}_1(m, k_z, k)$  and  $\varphi_1(m, k_z, \rho')$  are the Fourier transforms of  $\bar{p}(r, k)$  and  $\varphi(r')$ , respectively. Noticing that the right side of (4) is actually a Hankel transform, an inverse Hankel transform gives

$$\varphi_1(m, k_z, \rho') = \frac{8\pi C}{\beta v_s I_0} \int_0^\infty d\mu \frac{\mu \bar{p}_1(m, k_z, k) J_m(\mu\rho')}{k \bar{\eta}(k) H_m^2(\mu\rho)}, \quad |k| \geq |k_z|.$$

Applying a variable change of the integral variable from  $\mu$  to  $k$  to the above equation results in

$$\varphi_1(m, k_z, \rho') = \frac{8\pi C}{\beta v_s I_0} \int_{k_z}^\infty dk \frac{\bar{p}_1(m, k_z, k) J_m(\mu\rho')}{\bar{\eta}(k) H_m^2(\mu\rho)}, \quad |k| \geq |k_z|. \quad (5)$$

At last,  $\varphi_1(m, k_z, \rho')$  is inversely Fourier transformed with respect to  $m$  and  $k_z$  to yield  $\varphi(\phi', z', \rho')$ . Equation (5) gives an exact mapping relation between the spectrum of the collected signals and the spectrum of the distribution of microwave energy deposition and is the essence of our reconstruction method.

An exact reconstruction method for ultrasonic reflectivity imaging with a cylindrical scanning surface was given in [16]. However, our results are much simpler and more stable. In their equation A24,  $J_m(\mu r_0)$ , where  $r_0$  is the radius of the scanning cylindrical surface, appeared in the denominator and can be zero for some values of  $\mu$ ; consequently, this term can cause instability. In our (5),  $H_m^2(\mu\rho)$  appeared in the denominator, which cannot be zero for a finite  $\mu$ .

To summarize, the reconstruction procedure consists of the following steps.

- 1) The signal from the detector  $p(\phi, z, \bar{t})$  is Fourier transformed with respect to  $\bar{t}$  to yield  $\bar{p}(\phi, z, k)$ . Deconvolution with respect to the finite pulse length can be implemented immediately after the Fourier transform.
- 2)  $\bar{p}(\phi, z, k)$  is Fourier transformed with respect to  $z$  and  $\phi$ , giving  $\bar{p}_1(m, k_z, k)$ .
- 3) According to (5),  $\bar{p}_1(m, k_z, k)$  is mapped to  $\varphi_1(m, k_z, \rho')$ .
- 4)  $\varphi_1(m, k_z, \rho')$  is inversely Fourier transformed with respect to  $m, k_z$  to yield  $\varphi(\phi', z', \rho')$ .

### III. RESULTS AND DISCUSSION

To test our method, images from both numerically simulated and experimental data were reconstructed in a 2-D case. We chose the 2-D case rather than the three-dimensional (3-D) case to reduce the computational and experimental complexity. For the 2-D case, the reconstruction equation can be derived from

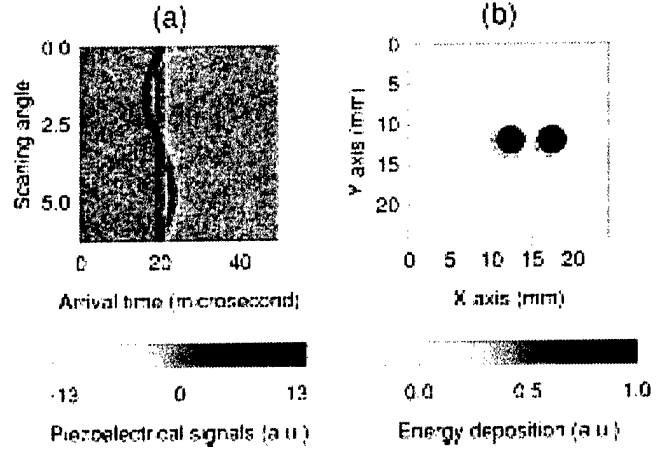


Fig. 1. The images (a) before and (b) after the reconstruction from the simulated data of two cylinders.

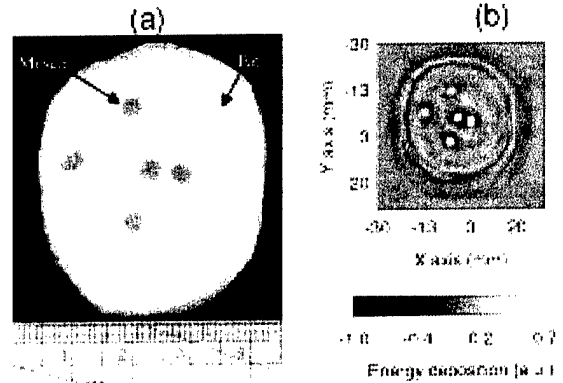


Fig. 2. (a) The cross section of a fat sample containing 5 pieces of muscle cylinders. (b) The reconstructed image from the experimental data.

(4) by replacing all  $k_z$  with zero. The extension of the conclusions of the 2-D case to a 3-D one is straightforward.

#### A. Numerical Simulation

The thermoacoustic imaging of two cylinders was numerically simulated, where the radius of each cylinder was 2 mm; the distance between the centers of the cylinders was 5 mm; and the center of one of the cylinders was positioned at the origin of the circle of detection. Cylinders were chosen because the analytical expression for their thermoacoustic signal is available [21]. In the simulations, the temporal-frequency range was from about 0 to 2 MHz, which was close to our experimental situation [14]. For the noiseless simulated data, the reconstruction is almost perfect. Therefore, we show only the results from noisy data. Fig. 1 shows the images before and after the reconstruction from the simulated data with introduced additive noise. The units for the signals and energy deposition in Figs. 1 and 2 are relative ones. Calibration of our system is needed to obtain an absolute measurement. The radius of the circle of detection was 30 mm; the angular scanning range was  $2\pi$  with 256 steps; and the thermoacoustic signals were sampled for 50  $\mu$ s at a sampling rate of 4 MHz. The signal-noise-ratio (SNR) of the raw data shown in Fig. 1(a) was 1. The reconstructed image shown in Fig. 1(b) is in good agreement with the real objects, whose

outlines are plotted as dotted circles in Fig. 1(b). The dimensions of the reconstructed cylinders are 4 mm along both the  $x$  and the  $y$  directions. The SNR of the reconstructed image is about 8, which is improved greatly compared with that of the raw data.

### B. Experiment Results

The experimental setup for 2-D TAT in a cylindrical configuration is the same as that in [12]. The sample is shown in Fig. 2(a), which was photographed after the experiment. Microwave pulses were delivered to the sample from below. The imaging plane was 2 cm above the bottom of the tissue sample. Above the plane, there is another layer of fat about 1 cm thick. The sample consisted of five muscle cylinders with a diameter of about 3 mm and a height of 6 mm. The muscle cylinders were surrounded by pork fat. The electrical property of interest to this imaging technique is the microwave attenuation coefficient of the medium at the experimental microwave frequency, 3 GHz. The microwave attenuation coefficients of fat and muscle are  $9 \text{ cm}^{-1}$  and  $1 \text{ cm}^{-1}$ , respectively. The microwave absorption in mineral oil can be neglected, compared with the absorption in fat and muscle. During the experiment, the transducer scanned around the sample at a radius of 7.1 cm from  $0^\circ$  to  $360^\circ$  with a step size of  $2.25^\circ$ . The thermoacoustic signals were sampled for  $60 \mu\text{s}$  at a sampling rate of 20 MHz. The time between the end of a microwave pulse and the acquisition of the thermoacoustic signal was between  $10 \mu\text{s}$  and  $20 \mu\text{s}$  in our system, depending on the distance of the transducer to the nearest sample surface.

Fig. 2(b) shows the reconstructed image from the experimental data. The reconstructed image is in good agreement with the real objects. The boundaries between the fat and the surrounding medium and the muscle cylinders are imaged clearly. However, it can be seen that the quality of the image decreases with the increasing distance of the objects from the center of the circle of detection. One possible reason is that the finite surface area of the detector, which has a 6-mm diameter in this experiment, may cause blurring of the image perpendicular to the radial direction, and this blurring is more serious when the object is farther from the center. Another possible reason is that the microwave field decreases when the radius increases in our irradiation configuration.

Our method can be applied to analyze the effect of the discrete sampling by the detector along the circle of detection on imaging. This can be illustrated by analyzing the signals from a point source located at radius  $\rho_1$ . According to (4)

$$\bar{p}_1(m, k) \propto J_m(k\rho_1). \quad (6)$$

Fig. 3 shows how  $J_m(k\rho_1)$  changes with  $m$ , where  $k = 8.37 \text{ mm}^{-1}$  (the wave number of a 2-MHz acoustic wave) and  $\rho_1 = 10 \text{ mm}$ . It is clear that  $J_m(k\rho_1)$  has considerable value until  $m \approx k\rho_1$ , where the Bessel function makes a transition from near-field behavior to far-field behavior. Therefore, it is safe to claim that, with respect to variable  $\phi$ ,  $\bar{p}(\mathbf{r}, k)$  is band-limited by  $k\rho_1$ . According to the Nyquist criteria, the number of scanning points per cycle should be at least  $2k\rho_1$  to avoid aliasing. In other words, for a fixed number of scanning points  $N$ , the maximum wave number before aliasing occurs

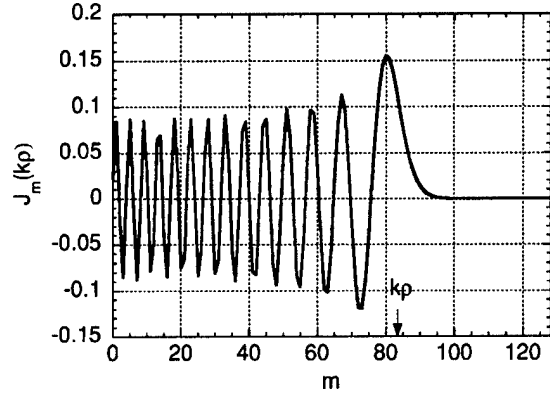


Fig. 3.  $J_m(k\rho_1)$  versus  $m$ , where  $k = 8.37 \text{ mm}^{-1}$  (the wave number of a 2 MHz acoustic wave) and  $\rho_1 = 10 \text{ mm}$ .

is  $k_{\text{max}} \approx N/(2\rho_1)$ . It can be seen that the maximum wave number is inversely proportional to  $\rho_1$ . For the same  $N$  and temporal spectrum of signal, the aliasing may be more serious for signals coming from sources at a greater radial distance than for those closer to the center. The above analysis also points out a way to produce an aliasing-free image from the data obtained by discrete detection. That is to apply a filter in the temporal-frequency domain to the spectrum of the temporal data with a stopband at about  $N/(2\rho_{\text{max}})$ , where  $\rho_{\text{max}}$  is the maximum radius of imaging range of interest. The application of the filter will decrease the resolution of the image; however, it can guarantee that there will be no aliasing in the image.

### C. Discussion

Since our method is implemented in the frequency domain using the fast Fourier transform (FFT) technique, the computational efficiency is much greater than if implemented in the time domain. The most time-consuming computation in the numerical reconstruction lies in (5), which is a Hankel transform. Fortunately, a quasi-fast algorithm for it, which is as efficient as a one-dimensional FFT, is available [22]. Following the methods in [11], our method can explicitly include and further eliminate the effect of many limitations from the experiment, such as the finite size of the detector surface, the microwave pulse length, and the finite response frequency range of the detector. Additionally, combining our method and the techniques in [16], a new exact reconstruction algorithm for 3-D ultrasonic reflectivity imaging with a cylindrical aperture can be derived. Finally, we would like to point out that the reconstruction methods reported in this paper and the two companion papers [11], [12] are also applicable to photoacoustic or optoacoustic tomography as well as other diffraction-based inverse source problem.

The size of tissue samples that can be imaged by our system is mainly limited by the safety standard on microwave power, the microwave frequency, the microwave irradiation configuration, the sensitivity of the ultrasonic transducer, the dynamic range of the preamplifier and sampling system, and the affordable imaging time. The effect of microwave frequency on the imaging depth was addressed in reference [13]. A microwave irradiation configuration that renders a uniform microwave irradiation within the sample will also increase the capacity of the system to image larger samples. A large dynamic range of the

preamplifier and the sampling system is necessary to accurately collect the thermoacoustic signals from both the surface and the inside of a sample. A more sensitive ultrasonic transducer and a longer imaging time can improve the signal-to-noise ratio of acoustic signals and make the weak signals from the inside of large samples detectable.

In our initial computation, the reconstruction of a single 2D image required about 2 min in a Dell Precision 330 computer (Intel Pentium 4 processor with a clock frequency of 1.5 GHz) with Matlab programs if there was no precomputation of Bessel and Hankel functions. However, our initial computation was aimed at verifying the proposed algorithm rather than demonstrating the computation efficiency. The proposed algorithm can be implemented with high computational efficiency as stated in the discussion section. For high computational efficiency, the program should be coded with languages such as C or Fortran, Bessel and Hankel functions should be precomputed, and the fast Hankel transform algorithm should be adopted. The evaluation of the computation efficiency of our algorithm is a topic for future studies.

#### IV. CONCLUSION

Using a new expansion of a spherical wave in the cylindrical coordinate system, we applied the Fourier transform and Hankel transform techniques to TAT with a cylindrical detection surface. The reconstruction algorithm is verified by both numerical simulations and experimental results in 2-D cases. The method was applied to analyze the effect of discrete sampling by the detector along the circle of detection on imaging; an aliasing-free reconstruction method for discrete sampling along the azimuth direction is proposed.

#### APPENDIX

The derivation of (2) will be presented here. The spherical wave  $G_k(\mathbf{r}, \mathbf{r}') = \exp(-ik|\mathbf{r} - \mathbf{r}'|)/(4\pi|\mathbf{r} - \mathbf{r}'|)$  is a solution to the wave equation with a point source

$$\nabla_r^2 G_k(\mathbf{r}, \mathbf{r}') + k^2 G_k(\mathbf{r}, \mathbf{r}') = -\delta(\mathbf{r} - \mathbf{r}'). \quad (\text{A1})$$

The solution can be expanded in terms of orthonormal functions of  $z$  and  $\phi$  in a cylindrical coordinate system

$$G_k(\mathbf{r}, \mathbf{r}') = \left(\frac{1}{2\pi}\right)^2 \sum_{m=-\infty}^{\infty} \int_{-\infty}^{\infty} dk_z g_m(k, k_z, \rho, \rho') \cdot \exp[im(\phi - \phi') + ik_z(z - z')]. \quad (\text{A2})$$

Substituting (A2) into (A1) results in an equation for the radial Green's function  $g_m$

$$\frac{1}{\rho} \frac{d}{d\rho} \left( \rho \frac{dg_m}{d\rho} \right) + \left( k^2 - k_z^2 - \frac{m^2}{\rho^2} \right) g_m = -\frac{\delta(\rho - \rho')}{\rho}. \quad (\text{A3})$$

When  $|k| < |k_z|$ , following the derivation of the series expansion of  $1/|\mathbf{r} - \mathbf{r}'|$  [20], one obtains a similar expansion for the spherical wave

$$g_m = I_m(|\mu|\rho') K_m(|\mu|\rho). \quad (\text{A4})$$

We next consider the case of  $|k| \geq |k_z|$  and  $k > 0$ . Noticing that when  $\rho \rightarrow \infty$ ,  $g_m$  behaves asymptotically as  $\exp[-i\mu(\rho - \rho')]$  ( $\rho > \rho'$  is implicit in our model), one can follow the derivation in [20] and obtain

$$g_m = \frac{\pi}{2i} J_m(\mu\rho') H_m^2(\mu\rho). \quad (\text{A5})$$

Similarly, for  $|k| \geq |k_z|$  and  $k < 0$

$$g_m = \frac{\pi i}{2} J_m(|\mu|\rho') H_m^1(|\mu|\rho). \quad (\text{A6})$$

Using the following identities of Bessel and Hankel functions [23]:

$$\begin{aligned} H_m^1(\mu\rho) &= -(-1)^m H_m^2(-\mu\rho), \\ J_m(\mu\rho) &= (-1)^m J_m(-\mu\rho) \end{aligned}$$

and combining (A2) and (A4)–(A6), we obtain (2).

#### REFERENCES

- [1] W. Joines, R. Jirtle, M. Rafal, and D. Schaeffer, "Microwave power absorption differences between normal and malignant tissue," *Radiation Oncol. Biol. Phys.*, vol. 6, pp. 681–687, 1980.
- [2] S. Chaudhary, R. Mishra, A. Swarup, and J. Thomas, "Dielectric properties of normal human breast tissues at radiowave and microwave frequencies," *Indian J. Biochem. Biophys.*, vol. 21, pp. 76–79, 1984.
- [3] W. Joines, Y. Zhang, C. Li, and R. Jirtle, "The measured electrical properties of normal and malignant human tissues from 50–900 MHz," *Med. Physics*, vol. 21, pp. 547–550, 1994.
- [4] L. E. Larsen and J. H. Jacobi, Eds., *Medical Applications of Microwave Imaging*. Piscataway, NJ: IEEE Press, 1986.
- [5] S. Caorsi, A. Frattoni, G. L. Gragnani, E. Nortino, and M. Pastorino, "Numerical algorithm for dielectric-permittivity microwave imaging of inhomogeneous biological bodies," *Med. Biol. Eng. Comput.*, vol. NS-29, pp. 37–44, 1991.
- [6] M. S. Hawley, A. Broquetas, L. Jofre, J. C. Bolomey, and G. Gaboriaud, "Microwave imaging of tissue blood content changes," *J. Biomed. Eng.*, vol. 13, pp. 197–202, 1991.
- [7] P. M. Meaney, K. D. Paulsen, and J. T. Chang, "Near-field microwave imaging of biologically-based materials using a monopole transceiver system," *IEEE Trans. Microwave Theory Tech.*, vol. 46, pp. 31–45, Jan. 1998.
- [8] R. A. Kruger, P. Liu, Y. R. Fang, and C. R. Appledorn, "Photoacoustic ultrasound (PAUS)-reconstruction tomography," *Med. Phys.*, vol. 22, pp. 1605–1609, 1995.
- [9] C. G. A. Hoelen, F. F. M. Demul, R. Pongers, and A. Dekker, "Three-dimensional photoacoustic imaging of blood vessels in tissue," *Opt. Lett.*, vol. 23, pp. 648–650, 1998.
- [10] G. Ku and L.-H. V. Wang, "Scanning thermoacoustic tomography in biological tissue," *Med. Phys.*, vol. 27, pp. 1195–1202, 2000.
- [11] Y. Xu, D. Feng, and L.-H. V. Wang, "Exact frequency-domain reconstruction for thermoacoustic tomography—II: Planar geometry," *IEEE Trans. Med. Imag.*, vol. 21, no. 7, pp. 823–828, July 2002.
- [12] M. Xu and L.-H. V. Wang, "Time-domain reconstruction for thermoacoustic tomography in a spherical geometry," *IEEE Trans. Med. Imag.*, vol. 21, no. 7, pp. 814–822, July 2002.
- [13] G. Ku and L.-H. V. Wang, "Scanning microwave-induced thermoacoustic tomography: Signal, resolution, and contrast," *Med. Phys.*, vol. 28, pp. 4–10, 2001.
- [14] Y. Xu and L.-H. V. Wang, "Signal processing in scanning thermoacoustic tomography in biological tissues," *Med. Phys.*, vol. 28, pp. 1519–1524, 2001.
- [15] H. Stark, J. W. Woods, I. Paul, and R. Hingorani, "Direct Fourier reconstruction in computer tomography," *IEEE Trans. Acoust. Speech Signal Processing*, vol. ASSP-29, pp. 237–245, 1981.
- [16] S. J. Norton and M. Linzer, "Ultrasonic reflectivity imaging in three dimensions: Exact inverse scattering solution for plane, cylindrical and spherical aperture," *IEEE Trans. Biomed. Eng.*, vol. BME-28, pp. 202–220, 1981.

- [17] K. Nagai, "A new synthetic-aperture focusing method for ultrasonic b-scan imaging by the Fourier transform," *IEEE Trans. Sonics Ultrason.*, vol. SU-32, pp. 531–536, 1985.
- [18] J. Lu, "Experimental study of high frame rate imaging with limited diffraction beams," *IEEE Trans. Ultrason. Ferroelect. Freq. Contr.*, vol. 45, pp. 84–97, Jan. 1998.
- [19] S. X. Pan and A. C. Kak, "A computational study of reconstruction algorithms for diffraction tomography: Interpolation versus filtered backprojection," *IEEE Trans. Acous. Speech Signal Processing*, vol. ASSP-31, pp. 1262–1275, 1983.
- [20] J. D. Jackson, *Classical Electrodynamics*. New York: Wiley, 1975.
- [21] G. J. Diebold, M. I. Khan, and S. M. Park, "Photoacoustic signatures of particulate matter: Optical production of acoustic monopole radiation," *Science*, vol. 250, pp. 101–104, 1990.
- [22] A. E. Siegman, "Quasi fast Hankel transform," *Opt. Lett.*, vol. 1, pp. 13–15, 1977.
- [23] M. Abramowitz and I. A. Stegun, *Handbook of Mathematical Functions*. New York: Dover, 1972.

# RF- and laser-induced thermoacoustic tomography

Minghua Xu, Xueding Wang and Lihong V. Wang

Optical Imaging Laboratory, Biomedical Engineering Program, Texas A&M University, 3120 TAMU, College Station, Texas 77843-3120

Email: [LWang@tamu.edu](mailto:LWang@tamu.edu); URL: <http://oilab.tamu.edu>

**Abstract** A study of pulsed-microwave-induced thermoacoustic tomography in biological tissues is presented. A backprojection algorithm based on rigorous theory is used to reconstruct the cross-sectional image from the thermoacoustic measurement in a circular configuration that encloses the sample under study. The results demonstrate the possibility of application in detecting small tumors buried in biological tissues using microwave absorption contrast and ultrasound spatial resolution. Finally, the method is compared with laser-induced thermoacoustic tomography.

© 2002 Optical Society of America

**OCIS Codes:** (170.5120) Photoacoustic imaging; (170.6960) Tomography

## 1. Introduction

Pulsed microwave-induced thermoacoustic tomography combines the advantages of both ultrasound spatial resolution and microwave absorption contrast [1]–[4]. With this technique, a very short microwave pulse ( $<1$  microsecond) heats a sample; the sample then absorbs the microwave energy in a confined time and simultaneously generates temporal thermoacoustic waves, which are strongly related to the locally absorbed microwave energy. The thermoacoustic signals have a wide frequency range up to  $\sim$  MHz and carry the information about microwave absorption distribution with millimeter spatial resolution. In practice, microwaves at 300 MHz  $\sim$  3 GHz with 0.1  $\sim$  1  $\mu$ s pulse are often adopted, which provide several centimeters penetration depths in biological tissues. Due to the bounded water and salt that exist in cancer cells, a tumor absorbs more microwave energy and generates more intense thermoacoustic waves than the surrounding tissues [5], [6]. The wide range of absorption values among various tissues makes it possible to achieve a high image contrast. In addition, the long penetration depth allows this technique to detect interior tumors.

In this paper, we present our study of pulsed-microwave-induced thermoacoustic tomography under a circular measurement configuration in biological tissues. A wide beam of short-pulse microwave energy is used to illuminate a sample from the bottom. An unfocused ultrasonic transducer with a small aperture is used to record the thermoacoustic signals. A backprojection method based on rigorous theory is used to reconstruct the cross-sectional image from the measured data. A phantom sample is investigated. The reconstructed image agrees with the original sample very well. Finally, the method is compared with laser-induced thermoacoustic tomography.

## 2. Method

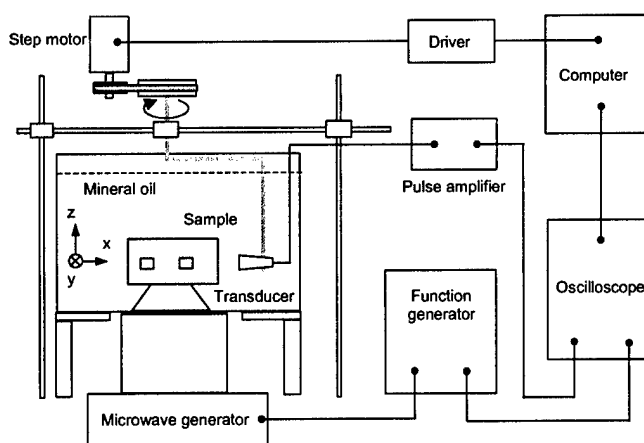


Fig. 1 Schematic of the circular measurement system

A schematic view of the circular measurement system for our study is shown in Fig. 1. A plexiglass container is filled with mineral oil. An unfocused transducer is immersed inside it and fixed on a rotation device. A step motor drives the rotation device and then moves the transducer scan around the sample on a horizontal x-y plane, where the transducer horizontally points to the rotation center. A sample is immersed inside the container and placed on a holder, which is made of thin plastic material that is transparent to the microwave. The transducer (V323, Panametrics) has a central frequency of 2.25 MHz, and a diameter of 6mm. The microwave pulses transmitted from a 3-GHz microwave generator have a pulse energy of 10 mJ and a pulse width of 0.5 $\mu$ s. A function generator

(Protek, B-180) is used to trigger the microwave generator, control its pulse repetition frequency, and synchronize the oscilloscope sampling. Microwave energy is delivered to the sample by a rectangular waveguide with a cross section of 72 mm × 34 mm. A personal computer is used to control the step. The signal from the transducer is first amplified through a pulse amplifier, then recorded and averaged 500 times by an oscilloscope (TDS640A, Tektronix), and finally transferred to a personal computer for imaging.

We assume the tissue to have inhomogeneous microwave absorption and a relatively homogeneous acoustic property. When the microwave pulse duration is  $< 1 \mu\text{s}$ , the heat diffusion's effect on the thermoacoustic wave in the tissue can be ignored. The speed of sound  $c$  in most soft tissue is relatively constant at  $\sim 1.5 \text{ mm}/\mu\text{s}$ . Suppose a delta illuminating function  $I_0 \delta(t)$  and a detected acoustic pressure  $p(\mathbf{r}_0, t)$  on the circular surface  $\mathbf{r} = \mathbf{r}_0 = (\rho_0, \phi_0, z_0)$  and time  $t$ . If challenged to detect small size tumors, we can safely remove the low-frequency component. In addition, the wavelengths of the high-frequency thermoacoustic waves are much smaller than the detecting distances between the thermoacoustic sources and the transducers. Under the above conditions, the spatial absorption function  $A(\mathbf{r})$  can be calculated by the following 2D surface integral in the cylindrical configuration

$$A(\rho, \phi, z) = -\frac{C_p}{2\pi c^4 \beta I_0} \int \int_{S_0} \rho_0 d\phi_0 dz_0 \sqrt{1 - \frac{(z_0 - z)^2}{|\mathbf{r} - \mathbf{r}_0|^2}} \frac{1}{t} \frac{\partial p(\mathbf{r}_0, t)}{\partial t} \Big|_{t = \frac{|\mathbf{r} - \mathbf{r}_0|}{c}}, \quad (1)$$

where  $\beta$  is the isobaric volume expansion coefficient and  $C_p$  is the heat capacity. The above reconstruction formula indicates that the cross-sectional image of any  $z$  plane is determined mainly by the data measured on the circle of the same  $z$  plane. In other words, if small absorption sources are located on a  $z$  plane, a set of circular measurement data on the same plane can be sufficient to yield a good cross-sectional image.

### 3. Results and Discussion

A phantom sample was imaged by our microwave-induced thermoacoustic tomography system. The measurement diagram and its cross-sectional photograph are shown in Fig. 2 (a) and (b), respectively. Three small absorbers, which were made of gelatin, salt and water, were buried inside a large fat base. The transducer rotationally scanned the sample from 0 to 360 degrees with a step size of 2.25 degree. The reconstructed image produced by our backprojection method is shown in Fig. 2 (c), which agrees with the original sample very well. The relative locations and sizes of those thermoacoustic sources perfectly match the buried objects in the original sample.

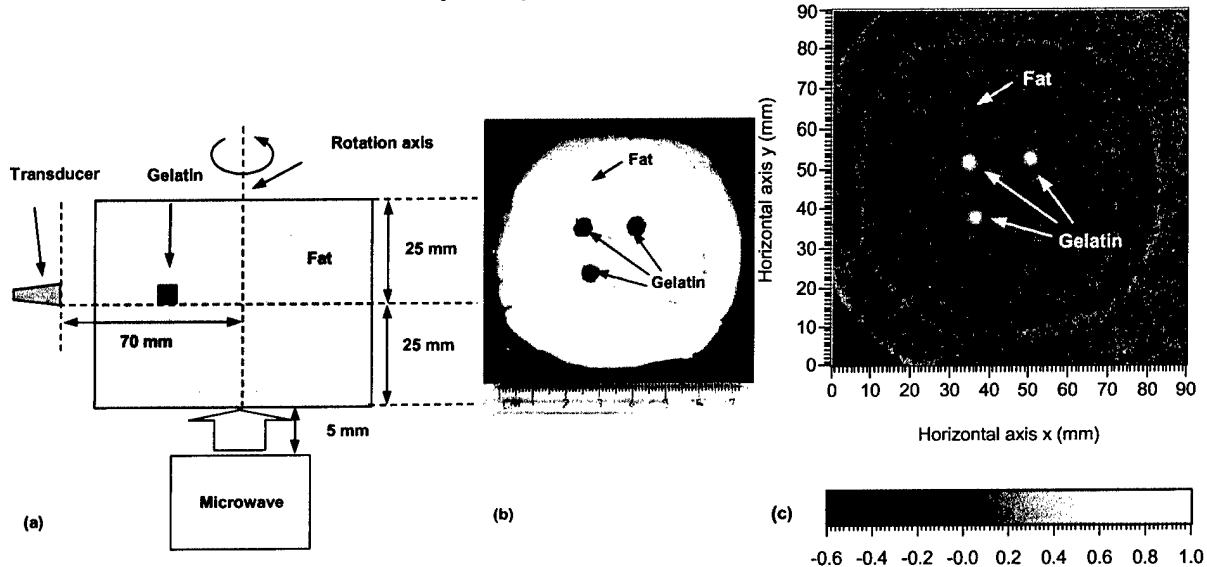


Fig. 2 (a) Diagram of the measurement scheme. (b) Photograph of the sample. (c) Reconstructed image.

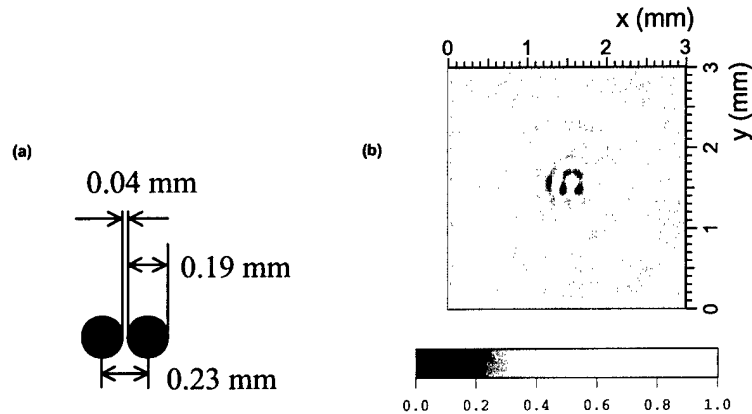


Fig. 3 (a) The schematic of two adjacent dots. (b) The reconstructed image.

For comparison, as Fig. 3 shows, an example of two black dots with a gap distance  $40\text{ }\mu\text{m}$  was imaged by traditional photoacoustic tomography, in which short laser pulses were used to illuminate the sample. A 10 MHz transducer was used to detect photoacoustic signal. Because the laser duration is only 4.7 ns, a higher frequency thermoacoustic signal was generated and a higher spatial resolution was obtained. However, the laser was not able to penetrate very deeply inside of the tissue.

### 3. Conclusion

We have presented our study on pulsed-microwave-induced thermoacoustic tomography by a circular measurement configuration in biological tissues. A backprojection algorithm is used to reconstruct the cross-sectional images. The reconstructed image of a phantom sample agrees with the original values very well. The result demonstrates that the circular measurement configuration combined with the backprojection method is a promising technique for use in detecting small tumors buried in biological tissues with microwave absorption contrast and ultrasound spatial resolution ( $\sim\text{mm}$ ). Alternatively, a pulsed-laser technique, which provides laser absorption contrast as well as high spatial resolution ( $\sim 50\text{ }\mu\text{m}$ ), can be employed as an illumination source to detect small tumors that are not very deeply buried.

### Acknowledgments

This project was sponsored in part by the U.S. Army Medical Research and Materiel Command Grant No. DAMD17-00-1-0455, the National Institutes of Health Grant No. R01 CA71980, the National Science Foundation Grant No. BES-9734491, and Texas Higher Education Coordinating Board Grant No. ARP 000512-0123-1999.

### References

- 1 R. A. Kruger, K. K. Kopecky, A. M. Aisen, D. R. Reinecke, G. A. Kruger and W. L. Kiser, "Thermoacoustic CT with radio waves: A medical imaging paradigm," *Radiology* **211**, pp. 275-278, 1999.
- 2 G. Ku and L.-H. V. Wang, "Scanning thermoacoustic tomography in biological tissues," *Med. Phys.* **27**, pp. 1195-1202, 2000.
- 3 G. Ku and L.-H. V. Wang, "Scanning microwave-induced thermoacoustic tomography: Signal, resolution, and contrast," *Med. Phys.* **28**, pp. 4-10, 2001.
- 4 M. H. Xu and G. Ku, and L.-H. V. Wang, "Microwave-induced thermoacoustic tomography using multi-sector scanning," *Med. Phys.* **29**, pp. 1958-1963, 2001.
- 5 S. Chaudhary, R. Mishra, A. Swarup, and J. Thomas, "Dielectric properties of normal human breast tissues at radiowave and microwave frequencies," *Indian Journal of Biochemistry and Biophysics* **21**, 76-79 (1984).
- 6 W. Joines, Y. Zhang, C. Li, and R. Jirtle, "The measured electrical properties of normal and malignant human tissues from 50-900 MHz," *Medical Physics* **21**, 547-550 (1994).